Structural and Multidisciplinary Optimization (2025) 68:245
https://doi.org/10.1007/s00158-025-04185-7

RESEARCH PAPER

Topology optimization of isotropic beam cross section accounting for stiffness and strength constraints

Zaiwei Lin[1] · Marco Morandini[1]

Received: 8 July 2025 / Revised: 19 October 2025 / Accepted: 21 October 2025
© The Author(s) 2025

Abstract
This paper presents a topology optimization framework for the design of isotropic beam cross section. The optimization question is formulated using the solid isotropic material with penalization method. The objective is to minimize the weight per unit of length of the beam, while the constraints can account not only for stiffness and strength requirements, but also for the position of the normal stress center and shear center, as well as the orientation of principal axis. During the optimization process, the cross-section analysis is performed by a dedicated two-dimensional finite element code, while the sensitivity information is efficiently computed by resorting to the adjoint method, significantly speeding up the optimization procedure. Numerical examples are presented to illustrate the effect of different constraint on the optimal cross-section topology. Finally, fully constrained optimizations are performed to demonstrate both the effectiveness of the proposed method and its applicability to practical cross-section design.

Keywords Beams · Cross-section stiffness matrix · Cross-section analysis · Topology optimization · Adjoint method

Nomenclature

a_k	Area of element k
$K^{\phi}_{44}, K^{\phi}_{55}, K^{\phi}_{45}$	Bending stiffness components wrt. the rotated system $(\boldsymbol{e}^{\phi}_1,\ \boldsymbol{e}^{\phi}_2)$
r_0	Filtering radius coefficient
r_{ik}	Distance between the centroids of elements i and k
w_k	Weighting factor used to filter $\boldsymbol{\rho}$ to $\tilde{\boldsymbol{\rho}}$
c^I, c^{I-1}	Multiplicative stress correction factor at iterations I and $I-1$
f	Optimization objective function
g_i	Optimization constraint function
p	Density penalization factor
p_N	Stress aggregation factor
p_s	Stress penalization factor
α	P-norm stress iterative update coefficient
$\bar{\sigma}_{PN}$	Iteratively updated P-norm stress function
β	Material density projection slope coefficient
η	Material density projection threshold coefficient
σ_{PN}	P-norm stress function
ϕ^p	Rotation angle defining the principal reference system
$\boldsymbol{B}$	Finite element strain–displacement matrix
$\boldsymbol{C}$	ANBA matrix used to build $\boldsymbol{H}$ and define the Neumann boundary condition
$\boldsymbol{D}$	Elastic constitutive matrix
$\boldsymbol{D}_0$	Solid material elastic matrix
$\boldsymbol{D}_i$	SIMP material elastic matrix of element i
$\boldsymbol{G}$	Beam strain transformation matrix
$\boldsymbol{K}$	Cross-sectional stiffness matrix
$\boldsymbol{K}'$	Decoupled cross-sectional stiffness matrix
$\boldsymbol{K}'_m$	Decoupled cross-sectional stiffness submatrix $\boldsymbol{K}_m$
$\boldsymbol{K}_t, \boldsymbol{K}_m, \boldsymbol{K}_c$	submatrices of cross-sectional stiffness matrix $\boldsymbol{K}$
$\boldsymbol{K}_v$	Vectorized stiffness matrix $\boldsymbol{K}$
$\boldsymbol{L}, \boldsymbol{R}$	matrices allowing to compute the internal resultant $\boldsymbol{\theta} = [\boldsymbol{t},\ \boldsymbol{m}]$ as a function of $\overline{\boldsymbol{u}}_{,3}$ and $\overline{\boldsymbol{u}}$, respectively; they are assembled from the corresponding element-level matrices $\boldsymbol{L}_i$ and $\boldsymbol{R}_i$
$\boldsymbol{M}, \boldsymbol{H}, \boldsymbol{E}$	ANBA matrices multiplying $\overline{\boldsymbol{u}}_{,33}$, $\overline{\boldsymbol{u}}_{,3}$, and $\overline{\boldsymbol{u}}$, respectively

Responsible Editor: Christian Gogu.

✉ Marco Morandini
marco.morandini@polimi.it

[1] Dipartimento di Scienze e Tecnologie Aerospaziali, Politecnico di Milano, via La Masa 34, 20156 Milano, Italy

Published online: 15 November 2025

$\boldsymbol{M}_i, \boldsymbol{C}_i, \boldsymbol{E}_i$	ANBA element-level matrices computed for element i
$\boldsymbol{P}_i$	Element i incidence matrix extracting the element displacement DOFs from the global vectors $\overline{\boldsymbol{u}}$ and $\overline{\boldsymbol{u}}_{,3}$
$\boldsymbol{Q}_d$	Matrix collecting the cross-section deformation modes
$\boldsymbol{S}$	$[\boldsymbol{0}\ \boldsymbol{I}]^T$
$\boldsymbol{V}$	Matrix allowing to compute the von Mises equivalent stress
$\boldsymbol{Y}$	Matrix defining the normal stress center and shear center
$\boldsymbol{Z}$	$[\boldsymbol{I},\ z]$
$\boldsymbol{c}_{10}, \boldsymbol{c}_{20}$	Starting eigenvectors for the traction and torsion chains: displacement along $\boldsymbol{e_3}$ and rotation around $\boldsymbol{e_3}$
$\boldsymbol{c}_{11}, \boldsymbol{c}_{21}$	Second generalized eigenvectors for traction and torsion chains
$\boldsymbol{c}_{30}, \boldsymbol{c}_{40}$	Starting eigenvectors for the bending chains: displacement along $\boldsymbol{e}_1$ and $\boldsymbol{e}_2$
$\boldsymbol{c}_{31}, \boldsymbol{c}_{32}$	Second and third generalized eigenvectors stemming from $\boldsymbol{c}_{30}$ after orthogonalization wrt the axial and torsion chains
$\boldsymbol{c}^0_{31}, \boldsymbol{c}^0_{41}$	Second generalized eigenvectors for the bending chains stemming from $\boldsymbol{c}_{30}$ and $\boldsymbol{c}_{40}$, respectively
$\boldsymbol{c}^0_{32}, \boldsymbol{c}^0_{42}$	Third generalized eigenvectors for the bending chains stemming from $\boldsymbol{c}_{30}$ and $\boldsymbol{c}_{40}$, respectively
$\boldsymbol{c}_{33}$	Fourth generalized eigenvector stemming from $\boldsymbol{c}_{30}$
$\boldsymbol{c}_{41}, \boldsymbol{c}_{42}$	Second and third generalized eigenvectors stemming from $\boldsymbol{c}_{40}$ after orthogonalization wrt the axial and torsion chains
$\boldsymbol{c}_{43}$	Fourth generalized eigenvector stemming from $\boldsymbol{c}_{40}$
$\boldsymbol{n}_1, \boldsymbol{n}_2$	Coefficients used to orthogonalize the generalized eigenvectors
$\boldsymbol{t}$	Internal section force resultant vector
σ_{allow}	Allowable equivalent stress
$\boldsymbol{e}^\phi_1, \boldsymbol{e}^\phi_2$	Unit vectors defining a reference system rotated by ϕ
$\boldsymbol{e}_1, \boldsymbol{e}_2$	Unit vectors on the cross-section plane
$\boldsymbol{e}_3$	Unit vector along the beam axis
$\overline{\boldsymbol{f}}_0, \overline{\boldsymbol{f}}_l$	Nodal forces vector at the two beam end surfaces, $x_3 = 0$ and $x_3 = l$
$\boldsymbol{k}_d$	Beam modal amplitude vector
$\boldsymbol{m}$	Internal section moment resultant vector
$\delta\boldsymbol{u}_0, \delta\boldsymbol{u}_l$	Virtual displacement at $x_3 = 0$ and $x_3 = l$, respectively
$\overline{\boldsymbol{u}}$	Nodal displacement vector
$\boldsymbol{u}$	Displacement vector
$\boldsymbol{x}^n$	Normal stress center
$\boldsymbol{x}^s$	Shear center
$\boldsymbol{z}$	Skew symmetric matrix built from the in-plane position
$\boldsymbol{\Lambda}_i$	Equations employed for the computation of the generalized eigenvectors
$\boldsymbol{\psi}$	Generalized beam strain
$\boldsymbol{\varepsilon}$	Small strain vector
$\boldsymbol{f}_0, \boldsymbol{f}_l$	External forces per unit of surface at the two beam end surfaces, $x_3 = 0$ and $x_3 = l$
$\boldsymbol{\theta}$	Internal section resultant vector
$\boldsymbol{\lambda}_i$	Adjoint matrices used for the computation of matrix $\boldsymbol{K}$ derivatives
$\boldsymbol{\lambda}^s_i$	Adjoint vectors used for the computation of σ_{PN} derivatives
$\overline{\boldsymbol{\rho}}$	Projected and filtered material density vector
$\tilde{\boldsymbol{\rho}}$	Filtered material density vector
$\boldsymbol{\rho}$	Material density vector
$\hat{\boldsymbol{\sigma}}^{vM}_i$	Relaxed von Mises element equivalent stress
$\hat{\boldsymbol{\sigma}}_i$	Relaxed element stress
$\boldsymbol{\sigma}^c_i$	Stress computed at the centroid of element i
$\boldsymbol{\sigma}_i$	Finite element stress
$\mathscr{D}$	In-plane strain derivation matrix
$\boldsymbol{\mathcal{L}}$	Augmented Lagrange system used for the computation of matrix $\boldsymbol{K}$ derivatives
$\boldsymbol{\mathcal{L}}^s$	Augmented Lagrange system used for the computation of σ_{PN} derivatives

1 Introduction

Beams are essential elements widely employed in civil engineering, aerospace, and numerous other technical domains. Their structural performance is largely governed by the topology of the cross sections, which directly affects the load-bearing capacity and deformation behavior. By optimizing the cross-sectional topology, engineers can significantly reduce material consumption while ensuring that the beam meets prescribed mechanical requirements, thereby achieving designs that are both structurally efficient and robust.

The problem of beam cross section optimization has been a longstanding focus in structural engineering research, particularly under the constraints of specified loading conditions and performance criteria (Makky and Ghalib 1979; Rozvany and Zhou 1991; Griffiths and Miles 2003). Shape optimization, based on the boundary evolution, provides an efficient framework for optimizing beam cross section, which allows for the identification of optimal cross section's boundary (Amir and Amir 2023) and facilitates the design of thin-walled members (Leng et al. 2011; Sharafi et al.

2014; Shimoda et al. 2020). However, while shape optimization offers targeted improvements, topology optimization presents a more versatile strategy, capable of exploring a broader design space and achieving more efficient use of materials.

For decades, topology optimization has been in the spotlight as a powerful and effective computational design method for determining the optimal material distribution within structures. It relies on numerical techniques to iteratively derive the optimal results while ensuring the satisfaction of constraints simultaneously. Nowadays, there are several popular numerical techniques used to carry out the topology optimization, such as the solid isotropic material with penalization method (SIMP) (Bendsoe and Sigmund 2013; Bendsøe 1989), evolutionary structural optimization method (ESO) (Huang and Xie 2010a, b), and level-set method (Wang et al. 2003; Van Dijk et al. 2013). The SIMP method is one of the most classical and widely used topology optimization technique. It formulates the optimization problem by weighting each element on the design domain with powered pseudo density ranging from 0 to 1. Nowadays, the SIMP method can be implemented to optimize the structures accounting for stiffness, vibration (Zargham et al. 2016), and instability (Gao and Ma 2015; Ferrari et al. 2021), with more difficult problems being composite optimization (Luo et al. 2020; Qiu et al. 2022) and multi-scale optimization (Wu et al. 2021).

Apart from these topics, stress-related topology optimization is of great importance, as it ensures structures remain safe from material failure under external loads. Nevertheless, incorporating stress into topology optimization poses significant challenges, primarily due to the singularity phenomenon and the local characteristics (Le et al. 2010; Yang et al. 2018). Singularity occurs because stress constraints associated to the zero-density elements prevent the optimization algorithm from finding the singular optimal points, which lie within the subspace of the full design space (Le et al. 2010). To alleviate the issue, stress relaxation techniques are often employed, such as epsilon-relaxed method (Cheng and Guo 1997) and qp relaxed method (Bruggi 2008), and thus enabling to reach the singular optimal points. Besides that, stress is a local quantity, which means each element must be evaluated to ensure that the stress level remains below the allowable limit. However, imposing stress constraint for each element will significantly increase the non-linearity of the optimization problem and the computation burden. To mitigate this, the local stress values can be incorporated into a global function through aggregation techniques such as the Kreisselmeier–Steinhauser (KS) approach, and the P-norm approach (Yang and Chen 1996). The global stress measure is widely used to formulate the stress constraints, providing an approximation of the maximum stress in the structure. However, it may fail to control the local stress level across the domain. Thus, the clustered technique (Holmberg et al. 2013) can be considered, in which all the stress evaluation points are separated into groups, with aggregation function applied within each group.

The first topology optimization work for the beam cross section was proposed in (Kim and Kim 2000), where an optimization model was developed in order to find the cross section with the largest bending and torsional stiffness under a constraint on the total mass. Subsequently, the authors addressed a new topology optimization problem that focuses on maximizing both the torsional and distortional rigidities (Kim and Kim 2002). Besides that, the cross-sectional torsion behavior has also been incorporated in another optimization study (Kostopoulos et al. 2025), in which the parameters governing the torsion and warping constants are optimized. Guo et al. (2021) proposed a topology optimization procedure for thin-walled cross sections that employs the moving morphable components (MMC) approach (Guo et al. 2014). The optimization objective is to find the minimum area, with the constraints set as bending and torsional moments of inertia. These works only deal with beam cross section, instead of constructing a beam model during the optimization process.

In other works, the optimization question is formulated with three dimensional models, accounting for specific boundary conditions and loads, while the beam cross sections are optimized. The eXtended Finite Element Method (XFEM) (Marzok et al. 2023; Marzok and Waisman 2023) enables the development of a topology optimization framework that is capable of optimizing the material distribution of extruded beam cross sections with the minimum mass, still satisfying stress, displacement, and buckling constraints (Marzok and Waisman 2024b). Another model based on XFEM (Marzok and Waisman 2024a) is aimed at obtaining the maximum fundamental natural frequency, while taking the mass and static compliance inequality constraints into the consideration. In a subsequent study, the same author proposed a different model toward the sizing and topology optimization of thin-walled beams based on the finite strip method (Marzok 2025). The optimal cross sections, derived from a set of line segments, are compared with that of the 3D continuous topology optimization. An optimization approach for beam cross section with buckling constraints has been developed (Nguyen et al. 2018). In their work, the linear buckling model is constructed with the finite prism method (a generalization of the finite strip method) in order to reduce the number of degrees of freedom.

Departing from the previous papers, beam models can also be employed in order to define a topology optimization problem. To this effect, however, the elastic properties of the beam need to be computed as a function of the cross section. Classical assumptions regarding the axial and bending displacement of the cross-section points, together with the assumption of an axial stress state, are adequate for characterizing the bending and axial properties of geometrically simple cross sections. However, these assumptions may lack accuracy when applied to beams with non-homogeneous or composite cross sections. This has led to the introduction of semi-analytical approaches for beam cross-section characterization, where the cross section is discretized using the finite element method while maintaining the displacement as an analytical function along the beam axis. Notable methods include ANBA (ANisotropic Beam Analysis) (Giavotto et al. 1983; Morandini et al. 2010), and VABS (Variational Asymptotic Beam Section analysis) (Cesnik and Hodges 1997; Hodges 2006), which allow for the computation of the 6×6 generalized stiffness matrix of an arbitrarily complex composite cross section. The resulting stiffness matrix can then be incorporated into any geometrically exact beam model, ensuring that the strain energy of the beam formulation matches that of the corresponding three-dimensional solid.

Some papers (Blasques and Stolpe 2012; Blasques 2014; Li et al. 2021; Liu et al. 2019, 2018, 2008; Ren et al. 2016) resort to the semi-analytical cross-section stiffness characterization developed by Giavotto (Giavotto et al. 1983) in order to compute the beam cross-section properties. Wang et al. (2020, 2021a, b) focused on the investigation of the coupled shape and topology optimization method for thin-walled beam structures. This methodology can be applied to non-prismatic wind turbine rotor blades. The same cross-section characterization procedure is adopted in (Blasques and Stolpe 2012), with a novel model that optimizes both the topology and laminate properties of composite beams. Not only it determines the cross-section shape, but also selects, for each element on the design domain, the suitable material from a set of candidates with different fiber orientations and fiber plane orientations. The same approach is then extended by accounting for beam eigenfrequency constraints (Blasques 2014). Liu at al. (2019) developed a model for the optimization of both the axial shape and cross section of non-prismatic beams. In this work, three different objective functions are considered, namely minimizing the structural compliance, maximizing the fundamental frequency, and maximizing the frequency gap, only accounting for volume constraint. Finally, in the concurrent topology optimization method for the stiffened plates developed by Li et al. (2021), the stiffeners are again modeled following Giavotto's work, so that the best layout and the cross-section topology of the stiffeners can be determined simultaneously.

Previous studies have provided a variety of optimization methods toward the design of beam cross sections, addressing different objectives and constraints. The mechanical response of a beam cross section is govern by a set of intrinsic properties, including bending and torsional stiffness, the position of the normal stress and shear centers, as well as the orientation of the principal axes. These properties are particularly critical in slender structures such as wind turbine and helicopter blades, as they dedicate the material distribution and significantly influence the aeroelastic stability of the structures. The constraints on centers have been explicitly considered in previous work (Blasques and Stolpe 2012). However, it may also be necessary to simultaneously control the principal axes orientation. Moreover, a topology optimization framework for beam cross section can become more versatile if the stiffness components can be considered individually, thereby providing a broader range of design options. In previous topology optimization works developed using Giavotto's beam theory, the strength assessment of the cross section has been neglected, representing another factor that should be accounted for during the optimization design of the cross section. Thus, compared with the previous studies, it is essential to develop a topology optimization framework that simultaneously incorporates either all or selected cross-sectional properties, while also accounting for the strength assessment.

This paper introduces a new topology optimization procedure for the design of isotropic beam cross section. The optimization problem is formulated based on the well-known SIMP method, with the objective of minimizing the weight per unit of length of the beam. Except for the strength evaluation, constraints can be defined based on design requirements of the cross-section properties, such as the minimum stiffness, allowable region of normal stress and shear centers, as well as the orientation of principal axis. Consequently, the framework can generate optimal results that not only meet the prescribed requirements, but also prevent material failure under external loads, providing a systematic approach for beam cross-section design. Furthermore, it is also shown, in this paper, how the different constraint individually affects the final optimization results.

In the present work, the beam cross-section analysis is performed with the latest version of the ANBA code (Morandini et al. 2010; Feil et al. 2020), ANBA4, with which the calculation of the central solutions requires solving a set of linear equation systems. This would make computing the derivative of the stiffness matrix by means of a direct differentiation method extremely costly. Thus, it is suitable to evaluate the derivative of cross-section properties, computed with ANBA4, through the adjoint method. This approach is adopted also in (Callejo et al. 2019; Han 2022), where the adjoint method allows to efficiently compute the derivative of the beam cross-section stiffness matrix with respect to the design variables.

The structure of this paper is arranged as follows. Section 2 introduces the beam cross-section analysis method by ANBA4. The topology optimization model is developed in the Sec. 3. Section 4 presents examples with different combination of constraints, while the last Sec. 5 gives the conclusion of the paper. The somewhat mechanical derivation of the adjoint solution procedure and the sensitivity validation are detailed in B and C, respectively.

2 Beam cross-section analysis

2.1 Beam central solutions

We consider a prismatic beam aligned along the $\boldsymbol{e}_3$ axis, with its cross section lying in the $\boldsymbol{e}_1 - \boldsymbol{e}_2$ plane, as in Fig. 1. The natural boundary conditions are external stress vectors acting on the two end surfaces of the beam, with the lateral surface remaining unloaded. The following derivation briefly summarizes the reference beam cross-section formulation first developed in (Giavotto et al. 1983), as re-formulated in (Morandini et al. 2010). Under the assumption of small deformation, the strain vector $\boldsymbol{\varepsilon} = [\varepsilon_{11}, \varepsilon_{22}, \gamma_{12}, \gamma_{13}, \gamma_{23}, \varepsilon_{33}]^T$ can be expressed as the sum of the derivative of the displacement $\boldsymbol{u}$ along the beam axis direction, denoted as $\boldsymbol{u}_{,3}$, and its derivative components on the cross section:

$$\boldsymbol{\varepsilon} = \boldsymbol{S}\boldsymbol{u}_{,3} + \mathscr{D}\boldsymbol{u}, \tag{1}$$

where the constant matrix $\boldsymbol{S}$ is given by $\boldsymbol{S} = \begin{bmatrix} \boldsymbol{0} & \boldsymbol{I} \end{bmatrix}^T$, with $\boldsymbol{0}$ and $\boldsymbol{I}$ denoting the 3×3 null and identity matrix, respectively. Besides that, the operator $\mathscr{D}$ is expressed as

$$\mathscr{D} = \begin{bmatrix} \frac{\partial}{\partial x_1} & 0 & 0 \\ 0 & \frac{\partial}{\partial x_2} & 0 \\ \frac{\partial}{\partial x_2} & \frac{\partial}{\partial x_1} & 0 \\ 0 & 0 & \frac{\partial}{\partial x_1} \\ 0 & 0 & \frac{\partial}{\partial x_2} \\ 0 & 0 & 0 \end{bmatrix}. \tag{2}$$

Assuming a linear elastic constitutive law, the virtual internal work $\delta\Pi_i$ and external work $\delta\Pi_e$ can be expressed as

$$\delta\Pi_i = \int_V [\delta\boldsymbol{u}_{,3}^T\boldsymbol{S}^T + \delta(\mathscr{D}\boldsymbol{u})^T]\boldsymbol{D}(\boldsymbol{S}\boldsymbol{u}_{,3} + \mathscr{D}\boldsymbol{u})\mathrm{d}V, \tag{3}$$

$$\delta\Pi_e = \int_A \delta\boldsymbol{u}_0^T\boldsymbol{f}_0\mathrm{d}A + \int_A \delta\boldsymbol{u}_l^T\boldsymbol{f}_l\mathrm{d}A \tag{4}$$

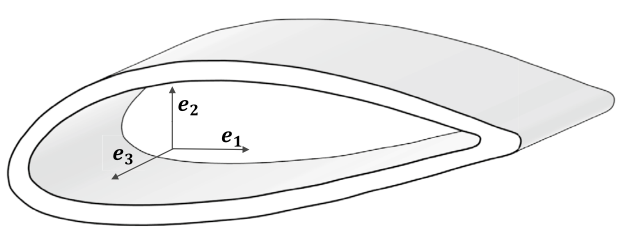

Fig. 1 Coordinate system of the beam cross section

in which, $\boldsymbol{D}$ is the elastic constitutive law matrix, $\delta\boldsymbol{u}_0$, $\delta\boldsymbol{u}_l$, $\boldsymbol{f}_0$, and $\boldsymbol{f}_l$ are the virtual displacements and external forces per unit of surface at the two beam end surfaces, $x_3 = 0$ and $x_3 = l$, respectively. The integration by part of the term involving $\delta\boldsymbol{u}_{,3}^T$ leads to the expression for $\delta\Pi_i$ as

$$\begin{aligned} \delta\Pi_i = & \left[\int_A \delta\boldsymbol{u}^T\boldsymbol{S}^T\boldsymbol{D}(\boldsymbol{S}\boldsymbol{u}_{,3} + \mathscr{D}\boldsymbol{u})\mathrm{d}A\right]_0^l \\ & - \int_V \delta\boldsymbol{u}^T\boldsymbol{S}^T\boldsymbol{D}(\boldsymbol{S}\boldsymbol{u}_{,33} + \mathscr{D}\boldsymbol{u}_{,3})\mathrm{d}V \\ & + \int_V \delta(\mathscr{D}\boldsymbol{u})^T\boldsymbol{D}(\boldsymbol{S}\boldsymbol{u}_{,3} + \mathscr{D}\boldsymbol{u})\mathrm{d}V \end{aligned} \tag{5}$$

The displacement field is then interpolated through finite element discretization on the cross section, with the beam axis direction remaining analytical. By imposing the virtual work balance with $\delta\Pi = \delta\Pi_i - \delta\Pi_e = 0$, the equilibrium equations system along the beam axis and natural boundary conditions at two ends can be expressed in matrix form as

$$\int_l \delta\bar{\boldsymbol{u}}^T(\boldsymbol{M}\bar{\boldsymbol{u}}_{,33} - \boldsymbol{H}\bar{\boldsymbol{u}}_{,3} - \boldsymbol{E}\bar{\boldsymbol{u}})\mathrm{d}x_3 = 0 \tag{6}$$

$$\delta\bar{\boldsymbol{u}}_0^T(\boldsymbol{M}\bar{\boldsymbol{u}}_{0,3} + \boldsymbol{C}^T\bar{\boldsymbol{u}}_0 - \bar{\boldsymbol{f}}_0) = 0, \quad \text{at}\, x_3 = 0 \tag{7}$$

$$\delta\bar{\boldsymbol{u}}_l^T(\boldsymbol{M}\bar{\boldsymbol{u}}_{l,3} + \boldsymbol{C}^T\bar{\boldsymbol{u}}_l - \bar{\boldsymbol{f}}_l) = 0, \quad \text{at}\, x_3 = l \tag{8}$$

where $\bar{\boldsymbol{u}}$ denotes the nodal displacements, $\bar{\boldsymbol{f}}_0$ and $\bar{\boldsymbol{f}}_l$ are the vectors of nodal forces at the two beam end surfaces, $x_3 = 0$ and $x_3 = l$, and matrix $\boldsymbol{H} = \boldsymbol{C} - \boldsymbol{C}^T$. Global matrices $\boldsymbol{M}, \boldsymbol{C}$, and $\boldsymbol{E}$ are assembled from element-level matrices $\boldsymbol{M}_i$, $\boldsymbol{C}_i$, and $\boldsymbol{E}_i$ as

$$\boldsymbol{M} = \sum_{i=1}^{N_e}\boldsymbol{M}_i, \; \boldsymbol{C} = \sum_{i=1}^{N_e}\boldsymbol{C}_i, \; \boldsymbol{E} = \sum_{i=1}^{N_e}\boldsymbol{E}_i, \tag{9}$$

with

$$\begin{aligned} \boldsymbol{M}_i &= \int_A \boldsymbol{N}^T\boldsymbol{S}^T\boldsymbol{D}\boldsymbol{S}\boldsymbol{N}\mathrm{d}A, \\ \boldsymbol{C}_i &= \int_A (\mathscr{D}\boldsymbol{N})^T\boldsymbol{D}\boldsymbol{S}\boldsymbol{N}\mathrm{d}A, \\ \boldsymbol{E}_i &= \int_A (\mathscr{D}\boldsymbol{N})^T\boldsymbol{D}\mathscr{D}\boldsymbol{N}\mathrm{d}A, \end{aligned} \tag{10}$$

in which $\boldsymbol{N}$ represents the element shape function matrix, and N_e denotes the number of finite elements on the cross section. Any standard two-dimensional FE can be used with ANBA, ranging from constant strain triangles to bicubic quadrilateral elements; the examples shown in this paper make use of bilinear quadrilateral elements, with the meshes covering the whole design domain. Each node has three degrees of freedom, one for each component of the three-dimensional displacement. Equations (7) and (8) simply state the equivalence of the normal stress vector and the applied force per unit of surface at the two beam ends, which are taken from granted in the following. Finally, from Eq. 6, the differential equations system that characterizes the beam cross-section response reads

$$\boldsymbol{M}\overline{\boldsymbol{u}}_{,33} - \boldsymbol{H}\overline{\boldsymbol{u}}_{,3} - \boldsymbol{E}\overline{\boldsymbol{u}} = 0. \tag{11}$$

The matrix $\boldsymbol{E}$ has a null-space spanned by four eigenvectors: $\boldsymbol{c}_{30}$, $\boldsymbol{c}_{40}$, and $\boldsymbol{c}_{10}$ represent rigid translations of the beam cross section along $\boldsymbol{e}_1$, $\boldsymbol{e}_2$, and $\boldsymbol{e}_3$ directions, while $\boldsymbol{c}_{20}$ describes a rotation around direction $\boldsymbol{e}_3$. The general solution of the second-order differential equations system Eq. (11) can be decomposed into the so-called extremity and central solutions, computed by solving the generalized eigenvalue problem ensuing from Eq. (11). The extremity solutions, governed by the nonzero eigenvalues, are characterized by deformation modes that decay exponentially along the beam axis. The central solution is associated with 12 null eigenvalues, which can be grouped into four families of polynomial solutions, representing the de Saint-Venant's response of the cross section for axial traction, torsion, and flexures along two in-plane directions, respectively. The polynomial solutions for axial traction and torsion correspond to two Jordan chains, each of length 2, with $\boldsymbol{c}_{10}$ and $\boldsymbol{c}_{20}$ from the null-space of $\boldsymbol{E}$ as the starting eigenvectors. Vectors $\boldsymbol{c}_{30}$ and $\boldsymbol{c}_{40}$ are the starting eigenvectors of the third and fourth Jordan chains, each of length 4, associated to the beam flexural behaviors. For a Jordan block with the starting eigenvector $\boldsymbol{c}_0$, the generalized eigenvector $\boldsymbol{c}_1$ can be computed by solving the linear equation system

$$\boldsymbol{E}\boldsymbol{c}_1 = -\boldsymbol{H}\boldsymbol{c}_0. \tag{12}$$

This allows to compute $\boldsymbol{c}_{11}$ that describes, for isotropic cross sections, the in-plane deformation due to the Poisson effect under axial deformation, and $\boldsymbol{c}_{21}$, representing the warping under torsion. While generalized eigenvectors $\boldsymbol{c}^0_{31}$ and $\boldsymbol{c}^0_{41}$, stemming from the bending Jordan chains, could be computed from Eq. (12), as they are analytically known, and represent rigid rotations of the cross section around $\boldsymbol{e}_2$ and $\boldsymbol{e}_1$, respectively. Generalized eigenvectors $\boldsymbol{c}^0_{32}$ and $\boldsymbol{c}^0_{42}$ can be computed by solving

$$\boldsymbol{E}\boldsymbol{c}_i = -\boldsymbol{H}\boldsymbol{c}_{i-1} + \boldsymbol{M}\boldsymbol{c}_{i-2},\ i \geq 2. \tag{13}$$

The Jordan chains initiated by $\boldsymbol{c}_{10}$ and $\boldsymbol{c}_{20}$ are limited to two terms, namely $\{\boldsymbol{c}_{11}, \boldsymbol{c}_{10}\}$ and $\{\boldsymbol{c}_{21}, \boldsymbol{c}_{20}\}$, respectively. This is because solving $\boldsymbol{E}\boldsymbol{c}_{12} = -\boldsymbol{H}\boldsymbol{c}_{11} + \boldsymbol{M}\boldsymbol{c}_{10}$ for $\boldsymbol{c}_{12}$ is impossible, since the right hand side $-\boldsymbol{H}\boldsymbol{c}_{11} + \boldsymbol{M}\boldsymbol{c}_{10}$ has nontrivial components along the nullspace of matrix $\boldsymbol{E}$; the same holds for the second chain, with both chains limited to the linear terms. Therefore, before reapplying Eq. (13) to compute the final generalized eigenvector $\boldsymbol{c}_{33}$ in the third Jordan chain, one needs to consider that, if $\boldsymbol{E}\boldsymbol{c}^0_{32} = -\boldsymbol{H}\boldsymbol{c}^0_{31} + \boldsymbol{M}\boldsymbol{c}_{30}$ and $\boldsymbol{E}\boldsymbol{c}_{11} = -\boldsymbol{H}\boldsymbol{c}_{10}$ are satisfied, then $\boldsymbol{E}(\boldsymbol{c}^0_{32} + \mu_1\boldsymbol{c}_{11}) = -\boldsymbol{H}(\boldsymbol{c}^0_{31} + \mu_1\boldsymbol{c}_{10}) + \boldsymbol{M}\boldsymbol{c}_{30}$ also holds, with μ_1 an arbitrary number; in the same way, one can add $\boldsymbol{c}_{21}$ and $\boldsymbol{c}_{20}$, since they satisfy $\boldsymbol{E}\boldsymbol{c}_{21} = -\boldsymbol{H}\boldsymbol{c}_{20}$. For this reason, before reapplying Eq. (13) to compute $\boldsymbol{c}_{33}$, one needs to modify the pair of vectors $\{\boldsymbol{c}^0_{32}, \boldsymbol{c}^0_{31}\}$ into $\{\boldsymbol{c}_{32}, \boldsymbol{c}_{31}\} = \{\boldsymbol{c}^0_{32} + \mu_1\boldsymbol{c}_{11} + \mu_2\boldsymbol{c}_{21}, \boldsymbol{c}^0_{31} + \mu_1\boldsymbol{c}_{10} + \mu_2\boldsymbol{c}_{20}\}$, with $\{\mu_{1,}\ \mu_2\}$ derived in such a way that the right hand side $-\boldsymbol{H}\boldsymbol{c}_{32} + \boldsymbol{M}\boldsymbol{c}_{31}$ has no component along $\boldsymbol{c}_{10}$ and $\boldsymbol{c}_{20}$. In order to achieve that, the coefficient $\boldsymbol{n}_1 = [\mu_1\ \mu_2]^T$ should be obtained by solving the linear system

$$\boldsymbol{A}\boldsymbol{n}_1 = \boldsymbol{b}_1 \tag{14}$$

in which,

$$\boldsymbol{A} = \begin{bmatrix} \boldsymbol{c}^T_{10} \\ \boldsymbol{c}^T_{20} \end{bmatrix} \begin{bmatrix} \boldsymbol{M} & -\boldsymbol{H} \end{bmatrix} \begin{bmatrix} \boldsymbol{c}_{10} & \boldsymbol{c}_{20} \\ \boldsymbol{c}_{11} & \boldsymbol{c}_{21} \end{bmatrix} \tag{15}$$

$$\boldsymbol{b}_1 = \begin{bmatrix} \boldsymbol{c}^T_{10} \\ \boldsymbol{c}^T_{20} \end{bmatrix} \begin{bmatrix} -\boldsymbol{M} & \boldsymbol{H} \end{bmatrix} \begin{bmatrix} \boldsymbol{c}^0_{31} \\ \boldsymbol{c}^0_{32} \end{bmatrix} \tag{16}$$

The generalized eigenvectors $\boldsymbol{c}^0_{31}$ and $\boldsymbol{c}^0_{32}$ can be updated according to

$$\begin{cases} \boldsymbol{c}_{31} = \boldsymbol{c}^0_{31} + [\,\boldsymbol{c}_{10}\ \ \boldsymbol{c}_{20}\,]\boldsymbol{n}_1, \\ \boldsymbol{c}_{32} = \boldsymbol{c}^0_{32} + [\,\boldsymbol{c}_{11}\ \ \boldsymbol{c}_{21}\,]\boldsymbol{n}_1. \end{cases} \tag{17}$$

The same orthogonalization procedure should be carried out for $\{\boldsymbol{c}^0_{42}, \boldsymbol{c}^0_{41}\}$ as well, leading to vectors $\{\boldsymbol{c}_{42}, \boldsymbol{c}_{41}\}$. This needs to compute an addition unknown vector $\boldsymbol{n}_2$, defined by solving a linear system with the same matrix $\boldsymbol{A}$ of Eq. (15) and the right-hand side

$$\boldsymbol{b}_2 = \begin{bmatrix} \boldsymbol{c}^T_{10} \\ \boldsymbol{c}^T_{20} \end{bmatrix} \begin{bmatrix} -\boldsymbol{M} & \boldsymbol{H} \end{bmatrix} \begin{bmatrix} \boldsymbol{c}^0_{41} \\ \boldsymbol{c}^0_{42} \end{bmatrix}. \tag{18}$$

Finally, the generalized eigenvectors $\boldsymbol{c}_{33}$ and $\boldsymbol{c}_{43}$ can be computed through Eq. (13), by employing $\{\boldsymbol{c}_{32}, \boldsymbol{c}_{31}\}$ and $\{\boldsymbol{c}_{42}, \boldsymbol{c}_{41}\}$, respectively.

2.2 Beam cross-section stiffness

The internal section force resultant vector $\boldsymbol{t}$ is defined as

$$\boldsymbol{t} = \int_A \begin{Bmatrix} \sigma_{13} \\ \sigma_{23} \\ \sigma_{33} \end{Bmatrix} \mathrm{d}A \tag{19}$$

comprising two shear force components t_1 and t_2 along $\boldsymbol{e}_1$ and $\boldsymbol{e}_2$, and the axial force component t_3, respectively. The internal section moment resultant vector $\boldsymbol{m}$ is defined as

$$\boldsymbol{m} = \int_A z^T \times \begin{Bmatrix} \sigma_{13} \\ \sigma_{23} \\ \sigma_{33} \end{Bmatrix} \mathrm{d}A, \tag{20}$$

with

$$z = \begin{bmatrix} 0 & 0 & -x_2 \\ 0 & 0 & x_1 \\ x_2 & -x_1 & 0 \end{bmatrix}. \tag{21}$$

Vector $\boldsymbol{m}$ has two bending moment components m_1 and m_2 and the torsional moment m_3. The internal section force and moment resultant vectors can be stacked into the 6×1 internal section resultant vector $\boldsymbol{\theta} = [\boldsymbol{t}; \boldsymbol{m}]$, where the $[\boldsymbol{t}; \boldsymbol{m}]$ notation means that the two vectors $\boldsymbol{t}$ and $\boldsymbol{m}$ are being stacked together in a single column.

Assuming that the beam deformation behavior is solely characterized by the central solutions, the cross-section nodal displacement vector $\bar{\boldsymbol{u}}$ and its derivative $\bar{\boldsymbol{u}}_{,3}$ can be expressed as $[\bar{\boldsymbol{u}}_{,3}; \bar{\boldsymbol{u}}] = \boldsymbol{Q}_d \boldsymbol{k}_d$, where the amplitude vector $\boldsymbol{k}_d$ is function of the internal resultant $\boldsymbol{\theta}$, and all the potential deformation modes are assembled in the matrix $\boldsymbol{Q}_d$ as follows:

$$\boldsymbol{Q}_d = \begin{bmatrix} \boldsymbol{c}_{10} & \boldsymbol{c}_{20} & \boldsymbol{c}_{31} & \boldsymbol{c}_{32} & \boldsymbol{c}_{41} & \boldsymbol{c}_{42} \\ \boldsymbol{c}_{11} & \boldsymbol{c}_{21} & \boldsymbol{c}_{32} & \boldsymbol{c}_{33} & \boldsymbol{c}_{42} & \boldsymbol{c}_{43} \end{bmatrix} \tag{22}$$

Vector $\boldsymbol{k}_d$ is not energetically conjugated to the internal resultant $\boldsymbol{\theta}$. Thus, we introduce the relationship $\boldsymbol{k}_d = \boldsymbol{G}\boldsymbol{\psi}$, where the transformation matrix $\boldsymbol{G}$ is computed in such a way to make $\boldsymbol{\psi}$ energetically conjugated to the internal resultant $\boldsymbol{\theta}$. Hence, recalling Eq. (3), the virtual internal work of the beam per unit of length becomes

$$\delta\Pi_i = \delta\boldsymbol{\psi}^T \boldsymbol{G}^T \boldsymbol{Q}_d^T \begin{bmatrix} \boldsymbol{M} & \boldsymbol{C}^T \\ \boldsymbol{C} & \boldsymbol{E} \end{bmatrix} \boldsymbol{Q}_d \boldsymbol{G}\boldsymbol{\psi}. \tag{23}$$

Following (Morandini et al. 2010), the internal resultant $\boldsymbol{\theta}$ computed over the discretized cross section is expressed as

$$\boldsymbol{\theta} = \begin{bmatrix} \boldsymbol{L}^T & \boldsymbol{R}^T \end{bmatrix} \boldsymbol{Q}_d \boldsymbol{k}_d = \begin{bmatrix} \boldsymbol{L}^T & \boldsymbol{R}^T \end{bmatrix} \boldsymbol{Q}_d \boldsymbol{G}\boldsymbol{\psi} \tag{24}$$

where matrices $\boldsymbol{L}$ and $\boldsymbol{R}$ are assembled from element-level matrices

$$\boldsymbol{L} = \sum_{i=1}^{N_e} \boldsymbol{L}_i, \ \boldsymbol{R} = \sum_{i=1}^{N_e} \boldsymbol{R}_i, \tag{25}$$

with

$$\boldsymbol{L}_i = \int_A \boldsymbol{N}^T \boldsymbol{S}^T \boldsymbol{D}\boldsymbol{S}\boldsymbol{Z} \mathrm{d}A, \tag{26}$$

$$\boldsymbol{R}_i = \int_A (\mathscr{D}\boldsymbol{N})^T \boldsymbol{D}\boldsymbol{S}\boldsymbol{Z} \mathrm{d}A, \tag{27}$$

where $\boldsymbol{Z} = [\boldsymbol{I}, z]$ and z is defined in Eq. 21.

The known resultant $\boldsymbol{\theta}$ on the cross section enables the evaluation of the coefficient $\boldsymbol{k}_d$ using Eq. 24, from which the stress in element i follows as

$$\boldsymbol{\sigma}_i = \boldsymbol{D}\boldsymbol{B}\boldsymbol{P}_i \boldsymbol{Q}_d \boldsymbol{k}_d, \tag{28}$$

where $\boldsymbol{B}$ is the finite element strain–displacement matrix and $\boldsymbol{P}_i$ selects the vertices values of the element i from the global displacement vector $\bar{\boldsymbol{u}}$ and $\bar{\boldsymbol{u}}_{,3}$.

Because of the relationship $\delta\Pi_i = \delta\boldsymbol{\psi}^T\boldsymbol{\theta}$ (Morandini et al. 2010), matrix $\boldsymbol{G}$ can be derived by solving the linear equation system

$$\boldsymbol{Q}_d^T \begin{bmatrix} \boldsymbol{M} & \boldsymbol{C}^T \\ \boldsymbol{C} & \boldsymbol{E} \end{bmatrix} \boldsymbol{Q}_d \boldsymbol{G} = \boldsymbol{Q}_d^T \begin{bmatrix} \boldsymbol{L} \\ \boldsymbol{R} \end{bmatrix} \tag{29}$$

This eventually enables the computation of the 6×6 cross-sectional stiffness matrix $\boldsymbol{K}$ as

$$\boldsymbol{K} = \begin{bmatrix} \boldsymbol{K}_t & \boldsymbol{K}_c \\ \boldsymbol{K}_c^T & \boldsymbol{K}_m \end{bmatrix} = \boldsymbol{G}^T \boldsymbol{Q}_d^T \begin{bmatrix} \boldsymbol{M} & \boldsymbol{C}^T \\ \boldsymbol{C} & \boldsymbol{E} \end{bmatrix} \boldsymbol{Q}_d \boldsymbol{G} \tag{30}$$

Further details associated with the computation of stiffness matrix can be found in (Morandini et al. 2010). The stiffness matrix $\boldsymbol{K}$ relates the internal resultant $\boldsymbol{\theta}$ to the cross-section deformation. Specifically, the 3×3 block $\boldsymbol{K}_t$ characterizes the resistance to shear and axial deformation caused by internal force $\boldsymbol{t}$, where K_{11} and K_{22} are the shear stiffness values along the $\boldsymbol{e}_1$ and $\boldsymbol{e}_2$ directions, K_{33} as the axial stiffness, and the off diagonal terms couple the axial and shear deformations. In the block $\boldsymbol{K}_m$, the diagonal terms K_{44} and K_{55} correspond to the bending stiffness about $\boldsymbol{e}_1$ and $\boldsymbol{e}_2$; K_{45} accounts for their coupling, and K_{66} represents the torsional stiffness. The block $\boldsymbol{K}_c$ couples the deformation caused by the force $\boldsymbol{t}$ and the moment $\boldsymbol{m}$; it can be partially eliminated by placing the original point of the coordinate system at either the normal stress center $\boldsymbol{x}^n$, which decouples the axial resultant from bending and is often referred to as the neutral axis, or at the shear center $\boldsymbol{x}^s$, which decouples the shear resultant from torsion. Using blocks $\boldsymbol{K}_t$ and $\boldsymbol{K}_c$, we define matrix $\boldsymbol{Y}$ as

$$\boldsymbol{Y} = -\boldsymbol{K}_t^{-1} \cdot \boldsymbol{K}_c. \tag{31}$$

The coordinate of both centers are stored, for an isotropic cross section, in the matrix $\boldsymbol{Y}$ with the shear center components given by $(x_1^s, x_2^s) = (-Y_{23}, Y_{13})$, and the normal stress center components equal to $(x_1^n, x_2^n) = (Y_{32}, -Y_{31})$. The normal stress center for a homogeneous and isotropic cross section coincides the mass center; in this paper, we keep using the normal stress center in the following expressions, without particularizing the formulation. After having computed matrix $\boldsymbol{Y}$, the decoupled stiffness matrix can be updated as

$$\boldsymbol{K}' = \begin{bmatrix} \boldsymbol{K}_t & 0 \\ 0 & \boldsymbol{K}'_m \end{bmatrix} = \begin{bmatrix} \boldsymbol{K}_t & 0 \\ 0 & \boldsymbol{K}_m - \boldsymbol{Y}^T \boldsymbol{K}_t \boldsymbol{Y} \end{bmatrix} \tag{32}$$

where the term K'_{66} is the torsional stiffness computed with respect to the $\boldsymbol{x}^s$, while K'_{44}, K'_{55}, and K'_{45} describe the cross-sectional bending behavior with respect to $\boldsymbol{x}^n$ in a reference frame aligned with $\boldsymbol{e}_1, \boldsymbol{e}_2$.

The stiffness terms related to bending can be further decoupled by introducing the principal axes. This can be achieved through a coordinate transformation that rotates the coordinate system such that the coupling term vanishes. The reference system, with origin located at $\boldsymbol{x}^n$ and axes aligned with the unit vectors $(\boldsymbol{e}_1, \boldsymbol{e}_2)$, can be rotated around axis $\boldsymbol{e}_3$ by the rotation angle ϕ, leading to a new system described by the rotated unit vectors $(\boldsymbol{e}_1^\phi, \boldsymbol{e}_2^\phi)$, as shown in the Fig. 2.

In the rotated coordinate system $(\boldsymbol{e}_1^\phi, \boldsymbol{e}_2^\phi)$,the bending stiffness sub-matrix can be updated as follows:

$$\begin{bmatrix} K_{44}^\phi & K_{45}^\phi \\ K_{45}^\phi & K_{55}^\phi \end{bmatrix} = \begin{bmatrix} \cos(\phi) & \sin(\phi) \\ -\sin(\phi) & \cos(\phi) \end{bmatrix} \begin{bmatrix} K'_{44} & K'_{45} \\ K'_{45} & K'_{55} \end{bmatrix} \begin{bmatrix} \cos(\phi) & -\sin(\phi) \\ \sin(\phi) & \cos(\phi) \end{bmatrix}. \tag{33}$$

In detail, K_{44}^ϕ and K_{55}^ϕ denote the bending stiffness along rotated axes $\boldsymbol{e}_1^\phi$ and $\boldsymbol{e}_2^\phi$, respectively, with K_{45}^ϕ the coupling term. Through this transformation, one can express the bending stiffness about each rotated axis based on the original bending stiffness components. The coordinate system decoupling the bending behavior can be found by imposing that $K_{45}^\phi = 0$, resulting in the corresponding rotation angle ϕ^p identified through

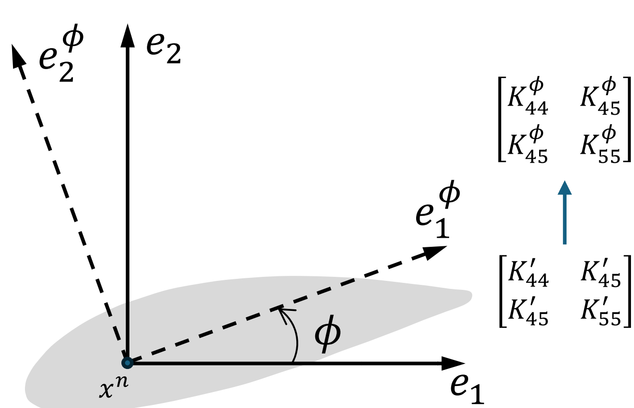

Fig. 2 Rotation of the coordinate system

$$\begin{cases} \tan(2\phi^p) = \frac{2K'_{45}}{K'_{44} - K'_{55}} & \text{if } K'_{44} \neq K'_{55}, \\ \cos(2\phi^p) = 0 & \text{if } K'_{44} = K'_{55}. \end{cases} \tag{34}$$

3 Topology optimization method for beam cross section

3.1 Formulation of the optimization question with the SIMP method

The present topology optimization problem is formulated via the SIMP method. The design domain is discretized into N_e planar elements, and each element i is assigned a "density" as design variable, denoted by $\rho_i \in [0, 1]$, where 0 and 1 stand for void and solid material, respectively. The vector of design variables is then represented as $\boldsymbol{\rho}$. To mitigate the checkerboard phenomenon (Díaz and Sigmund 1995), the density filtering technique proposed in (Wang et al. 2011) is applied to filter the vector $\boldsymbol{\rho}$ as $\widetilde{\boldsymbol{\rho}}$, with each component $\widetilde{\rho}_i$ determined as

$$\widetilde{\rho}_i = \frac{\sum_{k \in \Omega_i} w_k a_k \rho_k}{\sum_{k \in \Omega_i} w_k a_k}, \tag{35}$$

where Ω_i is the set of elements that lies in a circle of radius r_0, centered at the centroid of element i. The weighting factor for each element k is given by the multiplication of its area a_k and the coefficient $w_k = \max\left[0, (r_0 - r_{ik})\right]$, with r_{ik} denoting the distance between the centroids of elements i and k. While avoiding the checkerboard pattern, the filtering operation may potentially result in the presence of some elements with intermediate densities. In order to drive all the densities to either 0 or 1, the smoothed Heaviside projection method (Guest et al. 2004) is employed to project the filtered design variable vector $\widetilde{\boldsymbol{\rho}}$ to $\bar{\boldsymbol{\rho}}$ according to

$$\bar{\rho}_i = \frac{\tanh(\beta\eta) + \tanh(\beta(\widetilde{\rho}_i - \eta))}{\tanh(\beta\eta) + \tanh(\beta(1 - \eta))}, \tag{36}$$

where the parameter η denotes the projection threshold, and β controls the function slope.

According to the SIMP method, the elastic constitutive matrix of each element i, using the filtered and projected design variable $\bar{\rho}_i$, is computed as

$$\boldsymbol{D}_i = [\rho_{\min} + (1 - \rho_{\min})\bar{\rho}_i^p] \cdot \boldsymbol{D}_0, \tag{37}$$

where $\rho_{\min} = 10^{-6}$ is a small admissible value to prevent the singularity during the optimization iteration, and $p = 3$ is the penalization factor; $\boldsymbol{D}_0$ is the solid material elastic matrix. The cross-section analysis procedure outlined in Sec. 2 allows to compute both the cross-section stiffness matrix

$\boldsymbol{K}$ and the matrix $\boldsymbol{Y}$ as functions of design variables $\bar{\boldsymbol{\rho}}$, i.e., $\boldsymbol{K} = \boldsymbol{K}(\bar{\boldsymbol{\rho}})$ and $\boldsymbol{Y} = \boldsymbol{Y}(\bar{\boldsymbol{\rho}})$. Furthermore, the decoupled stiffness matrix $\boldsymbol{K}'$, the rotated bending stiffness terms ($K_{44}^{\phi}, K_{55}^{\phi}$), and the rotation angle ϕ^p defining the principal axes can be computed as function of the state of design variables $\bar{\boldsymbol{\rho}}$. These quantities can be used to define the design constraints, including minimum stiffness requirements, allowable range for the position of the normal stress center and shear center, and the orientation of the principal axes. In detail, the minimum shear stiffness and torsional stiffness requirements, denoted as $K_{22}^{\min}$ and $K_{66}^{\min}$, can be imposed, leading to the constraints as $K_{22} \geq K_{22}^{\min}$ and $K_{66}' \geq K_{66}^{\min}$. Similarly, a minimum bending stiffness $K_{44}^{\min}$ can be required either for K_{44}' or K_{44}^{ϕ}, namely the bending stiffness about $\boldsymbol{e}_1$ or $\boldsymbol{e}_1^{\phi}$, respectively. The position of $\boldsymbol{x}^n$ can be constrained in a specific region as: $x_1^{\min} \leq x_1^n \leq x_1^{\max}$, $x_2^{\min} \leq x_2^n \leq x_2^{\max}$, and corresponding constraints can likewise be enforced for the $\boldsymbol{x}^s$. Finally, the orientation of principal axes can also be confined with specific bounds. Recalling Eq. 34, the corresponding constraints can be set as

$$\tan(2\phi^{\min}) \leq \frac{2K_{45}'}{K_{44}' - K_{55}'} \leq \tan(2\phi^{\max}) \tag{38}$$

where, $\phi^{\min}$ and $\phi^{\max}$ are the lower and upper bounds of the rotation angle, respectively.

Stress constraint requires careful implementation for the avoidance of singularity, locality, and high non-linearity. In this paper we employ qp method (Bruggi 2008) to relax the stress at each evaluation point, and following (Holmberg et al. 2013), the relaxed stress $\hat{\boldsymbol{\sigma}}_i$ is computed as follows:

$$\hat{\boldsymbol{\sigma}}_i = \bar{\rho}_i^{p_s} \boldsymbol{\sigma}_i^c = \bar{\rho}_i^{p_s} \boldsymbol{D}_0 \boldsymbol{B} \boldsymbol{P}_i \boldsymbol{Q}_d \boldsymbol{k}_d, \tag{39}$$

where p_s is the stress penalization factor, and $\boldsymbol{\sigma}_i^c$ is the stress computed with $\boldsymbol{B}$ evaluated at the centroid of element i. The selection of p_s is of importance, because a smaller p_s can lead to excessive magnification of stress in low-density elements, while a bigger p_s may affect the degree of relaxation. Following previous studies (Le et al. 2010; Holmberg et al. 2013), we adopt the value $p_s = 0.5$ in this paper. The effect of different p_s values is briefly investigated in Appendix A. The von Mises equivalent stress $\hat{\boldsymbol{\sigma}}_i^{vM}$ is then calculated as

$$\hat{\sigma}_i^{vM} = \sqrt{\hat{\boldsymbol{\sigma}}_i^T \boldsymbol{V} \hat{\boldsymbol{\sigma}}_i}, \tag{40}$$

in which the constant coefficient matrix $\boldsymbol{V}$, written assuming that the components of $\hat{\boldsymbol{\sigma}}$ are now reordered as $\hat{\boldsymbol{\sigma}} = [\hat{\sigma}_{11}, \hat{\sigma}_{22}, \hat{\sigma}_{33}, \hat{\sigma}_{12}, \hat{\sigma}_{13}, \hat{\sigma}_{23}]^T$, is given by

$$\boldsymbol{V} = \begin{bmatrix} \tilde{\boldsymbol{V}} & \boldsymbol{0} \\ \boldsymbol{0} & 3\boldsymbol{I} \end{bmatrix}, \tag{41}$$

where

$$\tilde{\boldsymbol{V}} = \begin{bmatrix} 1 & -0.5 & -0.5 \\ -0.5 & 1 & -0.5 \\ -0.5 & -0.5 & 1 \end{bmatrix}. \tag{42}$$

The strength requirement is satisfied if each von Mises stress $\hat{\sigma}_i^{vM}$ remains below the allowable stress σ_{allow}. In this paper, a smooth and differentiable global P-norm stress function σ_{PN} (Yang and Chen 1996) is used to approximate the maximum von Mises equivalent stress level on the cross section as

$$\sigma_{PN} = \left(\sum_{i=1}^{N_e} \left(\hat{\sigma}_i^{vM} \right)^{p_N} \right)^{\frac{1}{p_N}}, \tag{43}$$

where the parameter p_N is the aggregation factor. The formulation of the P-norm ensures that the global stress σ_{PN} meets the condition $\sigma_{PN} \geq \max(\hat{\sigma}_1^{vM}, \hat{\sigma}_2^{vM}, \cdots \hat{\sigma}_{N_e}^{vM})$. In addition, σ_{PN} approaches the true maximum equivalent stress across the domain for $p_N \to \infty$. However, excessively large p_N value introduces high non-linearity, which may eventually result in numerical instability during the optimization process. Therefore, a smaller p_N is preferred to yield a smoother stress function σ_{PN}, despite the fact that it may lead to a more conservative constraint relative to the admissible limit. This is because the P-norm stress function σ_{PN} tends to overestimate the maximum stress. This effect is particularly evident in beam cases, where the stress distribution across the cross section is relatively smooth, so that the maximum stress is not substantially higher than those attained in the different positions of the cross section. To address this, the global P-norm stress function is iteratively updated, at each optimization step I, by a multiplicative correction factor c^I so that

$$\bar{\sigma}_{PN} = c^I \cdot \sigma_{PN} \leq \sigma_{\text{allow}}. \tag{44}$$

Following (Le et al. 2010), and starting from an initial value $c^1 = 1$, c^I is updated according to

$$c^I = \alpha \cdot \frac{\max(\hat{\sigma}_i^{vM})_{I-1}}{\sigma_{PN}^{I-1}} + (1-\alpha) \cdot c^{I-1} \quad \text{for } I > 1 \tag{45}$$

where c^{I-1}, σ_{PN}^{I-1}, and $\max(\hat{\sigma}_i^{vM})_{I-1}$ denote the correction factor, P-norm stress value, and the maximum von Mises stress at previous step, respectively, and $\alpha = 0.5$ is a fixed parameter.

The optimization goal is to minimize the structure weight while assuring the satisfaction of selected constraints $g_i(\bar{\boldsymbol{\rho}})$, which include minimum stiffness requirements, the permissible regions for the normal stress center and the shear center and orientation of principal axis, and strength constraint ($\bar{\sigma}_{PN} \leq \sigma_{\text{allow}}$). For a cross section made with an isotropic material, the objective function can be equivalently redefined as the area ratio of the cross section,

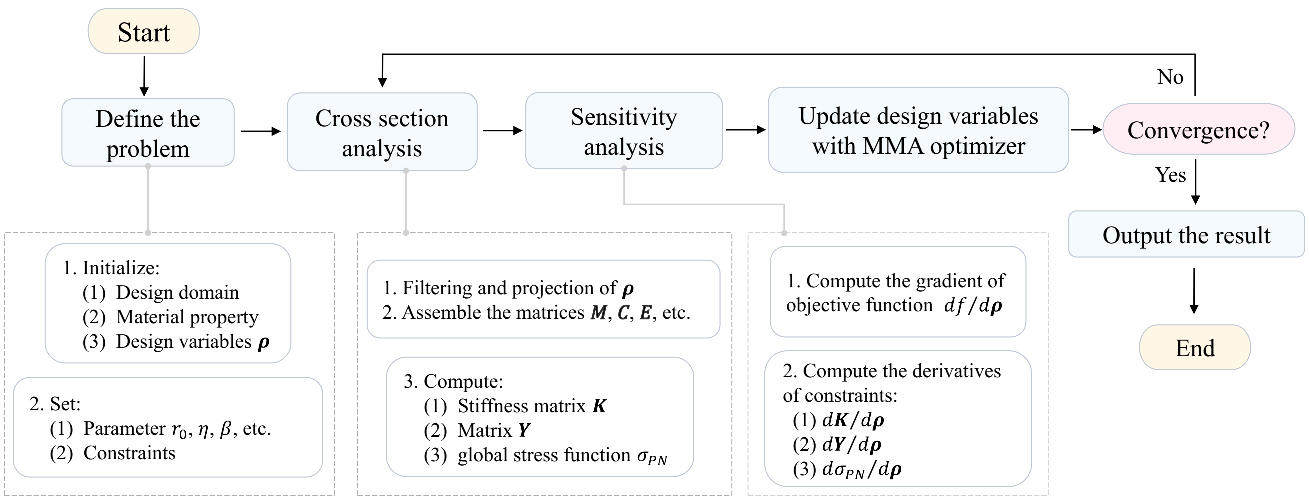

Fig. 3 Flowchart of the optimization procedure

$$f(\bar{\boldsymbol{\rho}}) = \frac{\sum_{i=1}^{N_e} a_i \bar{\rho}_i}{\sum_{i=1}^{N_e} a_i}. \tag{46}$$

Therefore, the overall optimization problem is presented as

$$\begin{cases} \underset{\boldsymbol{\rho}}{\text{minimize}} \ f(\bar{\boldsymbol{\rho}}) \\ \text{subject to } \ g_i(\bar{\boldsymbol{\rho}}) \le 0, \\ \qquad\qquad\quad 0 \le \rho_j \le 1, \end{cases} \tag{47}$$

The flowchart of the optimization procedure is summarized in Fig. 3. The optimization parameters are initialized, with both the design domain and constraints defined. The first step in each iteration is to assemble matrices $\boldsymbol{M}$, $\boldsymbol{C}$, $\boldsymbol{E}$, $\boldsymbol{L}$, and $\boldsymbol{R}$. Then, the cross-section analysis is performed. The sensitivity information of the objective function and constraints are computed, following the procedure discussed in the next Sec. 3.2. Finally, the optimization problem at the current step is solved using the Method of Moving Asymptotes (MMA) optimizer (Svanberg 1987), with a reduced move limit enforced to maintain the stability. The program terminates when the maximum design variable change is smaller than 0.001.

3.2 Sensitivity analysis

The MMA optimizer requires the first-order sensitivity information of the objective function and constraints to update design variables $\boldsymbol{\rho}$. For a scalar function $g(\bar{\boldsymbol{\rho}})$ dependent on the filtered and projected design variables vector $\bar{\boldsymbol{\rho}}$, its gradient with respect to the original design variable vector $\boldsymbol{\rho}$ is computed with the chain rule as

$$\frac{\mathrm{d}g(\bar{\boldsymbol{\rho}})}{\mathrm{d}\boldsymbol{\rho}} = \frac{\mathrm{d}g(\bar{\boldsymbol{\rho}})}{\mathrm{d}\bar{\boldsymbol{\rho}}} \frac{\mathrm{d}\bar{\boldsymbol{\rho}}}{\mathrm{d}\tilde{\boldsymbol{\rho}}} \frac{\mathrm{d}\tilde{\boldsymbol{\rho}}}{\mathrm{d}\boldsymbol{\rho}} \tag{48}$$

As a result of the application of the projection function and filtering technique for design variable $\boldsymbol{\rho}$, the terms $\partial\bar{\rho}_i/\partial\tilde{\rho}_i$ and $\partial\tilde{\rho}_i/\partial\rho_j$ are computed as

$$\frac{\partial\bar{\rho}_i}{\partial\tilde{\rho}_i} = \frac{\beta - \beta \tanh^2(\beta(\tilde{\rho}_i - \eta))}{\tanh(\beta\eta) + \tanh(\beta(1-\eta))}, \tag{49}$$

$$\frac{\partial\tilde{\rho}_i}{\partial\rho_j} = \frac{w_j a_j}{\sum_{k\in\Omega_i} w_k a_k} \tag{50}$$

After having computed $\mathrm{d}g(\bar{\boldsymbol{\rho}})/\mathrm{d}\bar{\boldsymbol{\rho}}$, the calculation of $\mathrm{d}g(\bar{\boldsymbol{\rho}})/\mathrm{d}\boldsymbol{\rho}$ from Eqs. (48-50) is straightforward. There are two computational methods that are widely adopted for the sensitivity analysis: the direct method and the adjoint method. The direct method explicitly computes the derivative for each design variable, making it appropriate for functions with straightforward composition. This is the case for the derivative of the objective function f with respect to the design variable $\bar{\rho}_i$, which can be directly obtained through

$$\frac{\partial f}{\partial\bar{\rho}_i} = \frac{a_i}{\sum_{k=1}^{N_e} a_k} \tag{51}$$

The sensitivity analysis of stiffness matrix $\boldsymbol{K}$, instead, is more complex due to the mandatory computation of generalized eigenvectors from Eq. (11). With the direct method, the derivative of $\boldsymbol{K}$ with respect to each design variable $\bar{\rho}_i$ can be computed using Eq. (29) and Eq. (30) as

Table 1 Direct and adjoint sensitivity analysis run time

N_e	400	625	900	1225	1600	2025	2500	3025	3600	4225	4900
Adjoint / s	0.140	0.185	0.234	0.301	0.382	0.382	0.582	0.703	0.853	1.009	1.214
Direct / s	0.599	1.377	2.612	4.794	8.387	13.320	21.270	32.755	47.956	67.266	97.148

$$
\begin{aligned}
\frac{\partial \boldsymbol{K}}{\partial \bar{\rho}_i} = {} & \frac{\partial \boldsymbol{T}^T}{\partial \bar{\rho}_i}\boldsymbol{Q}_d\boldsymbol{G} - \boldsymbol{G}^T\boldsymbol{Q}_d^T\frac{\partial \boldsymbol{W}}{\partial \bar{\rho}_i}\boldsymbol{Q}_d\boldsymbol{G} + \boldsymbol{G}^T\boldsymbol{Q}_d^T\frac{\partial \boldsymbol{T}}{\partial \bar{\rho}_i} \\
& + \boldsymbol{T}^T\frac{\partial \boldsymbol{Q}_d}{\partial \bar{\rho}_i}\boldsymbol{G} - \boldsymbol{G}^T\frac{\partial \boldsymbol{Q}_d^T}{\partial \bar{\rho}_i}\boldsymbol{W}\boldsymbol{Q}_d\boldsymbol{G} \\
& - \boldsymbol{G}^T\boldsymbol{Q}_d^T\boldsymbol{W}\frac{\partial \boldsymbol{Q}_d}{\partial \bar{\rho}_i}\boldsymbol{G} + \boldsymbol{G}^T\frac{\partial \boldsymbol{Q}_d^T}{\partial \bar{\rho}_i}\boldsymbol{T},
\end{aligned}
\tag{52}
$$

where $\boldsymbol{T}$ is a short for $[\boldsymbol{L};\boldsymbol{R}]$, $\boldsymbol{W}$ is a short for $\begin{bmatrix} \boldsymbol{M} & \boldsymbol{C}^T \\ \boldsymbol{C} & \boldsymbol{E} \end{bmatrix}$. Equation (52) involves the derivatives of the generalized eigenvectors with respect to $\bar{\rho}_i$, i.e., $\partial \boldsymbol{Q}_d/\partial \bar{\rho}_i$, thus requiring the solution of 12 linear equation systems (of which only six are computationally expensive) with respect to a single variable $\bar{\rho}_i$.

In this case, the adjoint method (Han 2022; Callejo et al. 2019) is the ideal choice to conduct the sensitivity analysis of the stiffness matrix $\boldsymbol{K}$, and leads to a substantially cheaper algorithm. The key point of the adjoint method is to construct an augmented Lagrange function that incorporates all the involved constraints. The necessity to compute the derivative of the state variables is avoided through the identification of a suitable adjoint variable λ_i for each constraint. Regardless of the number of design variables included in the model, only a constant number of linear systems is required in order to compute the adjoint variables λ_i. The algorithm for the computation of the stiffness matrix derivative is detailed in Appendix B.

Table 1 compares, as a function of the number of elements N_e, the run time required to perform the sensitivity analysis of the stiffness matrix by means of the adjoint and direct methods, highlighting the different scaling of the two approaches; results in the table were obtained by setting all the design variables equal to 0.5, and averaged over five runs performed on a desktop pc.

After having computed the derivative of the stiffness matrix, the derivative of matrix $\boldsymbol{Y}$, defining the shear and normal stress centers, is equal to

$$
\frac{\partial \boldsymbol{Y}}{\partial \bar{\rho}_i} = -\boldsymbol{K}_t^{-1}\frac{\partial \boldsymbol{K}_c}{\partial \bar{\rho}_i} - \boldsymbol{K}_t^{-1}\frac{\partial \boldsymbol{K}_t}{\partial \bar{\rho}_i}\boldsymbol{Y}. \tag{53}
$$

where one can extract the sensitivity information regarding the coordinates of normal stress and shear centers. By making use of Eq. (53), the derivative of $\boldsymbol{K}'_m$ can be obtained through

$$
\frac{\partial \boldsymbol{K}'_m}{\partial \bar{\rho}_i} = \frac{\partial \boldsymbol{K}_m}{\partial \bar{\rho}_i} - \frac{\partial \boldsymbol{Y}^T}{\partial \bar{\rho}_i}\boldsymbol{K}_t\boldsymbol{Y} - \boldsymbol{Y}^T\frac{\partial \boldsymbol{K}_t}{\partial \bar{\rho}_i}\boldsymbol{Y} - \boldsymbol{Y}^T\boldsymbol{K}_t\frac{\partial \boldsymbol{Y}}{\partial \bar{\rho}_i}. \tag{54}
$$

The gradient of the global stress function $\mathrm{d}\sigma_{PN}/\mathrm{d}\bar{\boldsymbol{\rho}}$ should also be computed using the adjoint method in order to avoid computing the derivative of generalized eigenvectors to each design variable, and is detailed in Appendix B as well. Using the derivatives provided above, the sensitivity information for the constraints can be readily computed. For brevity, their explicit expressions are not included here.

The sensitivity expressions obtained using the adjoint method are validated by comparing them with those obtained using finite differences in Appendix C.

4 Case studies

This section applies the proposed topology optimization framework to different problems with increasing complexity. Two distinct design domains are considered: a 120× 120 mm square domain and a fx83w227-il airfoil profile, with the chord length of 1 m. The square domain, shown in Fig. 4a, is discretized into a 60× 60 mesh of equal square elements, with its geometric center serving as the coordinate origin. As for the profile, only 75% of the chord is meshed, considering the trailing edge as non-structural, and leading to a design domain composed of 5383 quadrilateral finite elements, as shown in Fig. 4b. To simplify constraint imposition on the coordinates of $\boldsymbol{x}^n$ and $\boldsymbol{x}^s$, all nodes of the profile mesh are located in the first quadrant of the coordinate system.

The isotropic material properties are as follows: elastic modulus $E_0 = 70$ GPa, and Poisson ratio $\nu = 0.3$. The projection parameters η and β of Eq. (36) are set to $\eta = 0.5$ and $\beta = 20$. The filter radius is assigned values of $r_0 = 6$ and $r_0 = 12$ for the square and profile domains, respectively. Each design variable ρ_i is initialized as 0.5 to avoid the occurrence of excessively small stiffness values caused by the penalization on elastic modulus during the initial optimization steps. Finally, the parameter p_N of Eq. (43) is set to $p_N = 8$, consistently with (Holmberg et al. 2013).

The following subsections will evaluate the effectiveness of the optimization procedure with different setting of constraints, and investigate how they influence final optimization results with increasing complexity. In addition, to explicitly illustrate the properties of the optimal cross

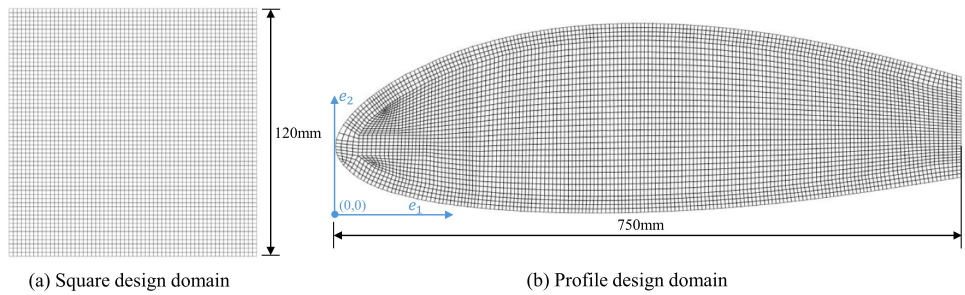

Fig. 4 Finite element mesh of the design domains; **a** square domain; **b** profile domain

section, the positions of the normal stress and shear centers as well as the principal axes will be displayed, with the exception of the results for the square domain. If no constraints associated with these features are prescribed, they will be displayed in gray.

4.1 Shear and bending stiffness constraints

Using the square design domain, the first group of examples considers different combinations of shear and bending stiffness constraints. Each optimization design is obtained by adding a minimum shear stiffness $K_{22}^{\min}$ and a minimum bending stiffness $K_{44}^{\min}$ as constraints, resulting in the optimization problem

$$\begin{cases} \underset{\rho}{\text{minimize}} \;\; f(\bar{\boldsymbol{\rho}}) \\ \text{subject to} \;\; K_{22}^{\min} - K_{22}(\bar{\boldsymbol{\rho}}) \leq 0, \\ \qquad\qquad\quad K_{44}^{\min} - K'_{44}(\bar{\boldsymbol{\rho}}) \leq 0, \\ \qquad\qquad\quad 0 \leq \rho_i \leq 1. \end{cases}$$

Figure 5 reports the typical variation of the objective function f and of both stiffness values throughout the optimization process. The shear stiffness K_{22} and the bending stiffness K'_{44} eventually reach their respective minimum values of $K_{22}^{\min} = 7E7$ N and $K_{44}^{\min} = 8E11$ Nmm^2, with the objective function converging to $f = 0.3973$.

Figure 6a compares cross-section topologies obtained with the same minimum shear stiffness $K_{22}^{\min} = 8\text{E}7$ N but different setting on the bending stiffness constraint. Conversely, Fig. 6b demonstrates the impact of different shear stiffness constraint values with a fixed minimum bending stiffness of $K_{44}^{\min} = 5\text{E}11$ Nmm^2. In detail, all the present cross sections have the shear and bending stiffness values

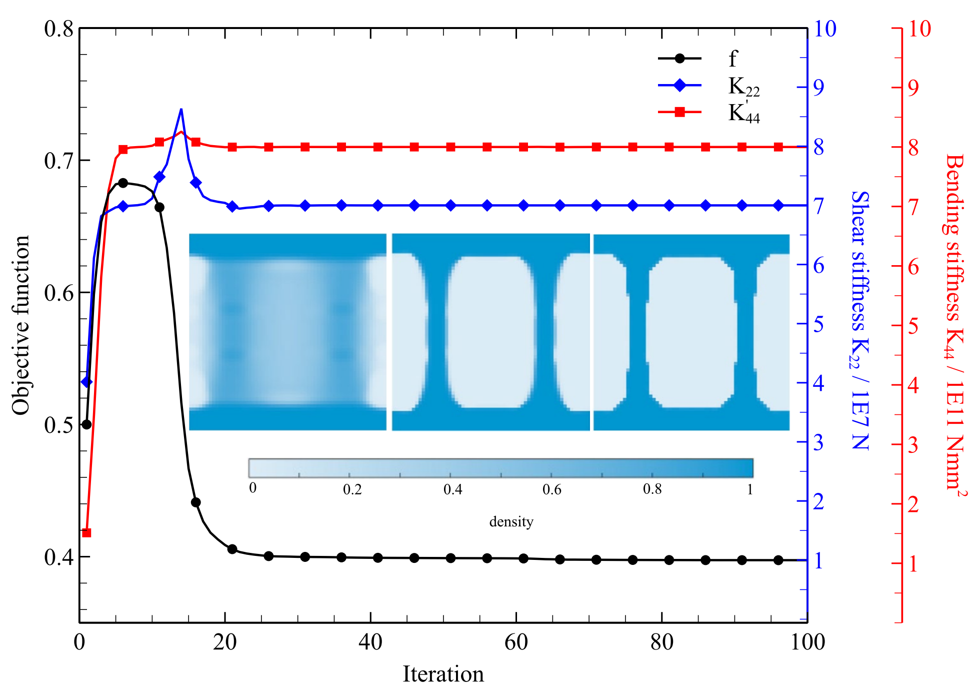

Fig. 5 Convergence of the optimization, square domain with $K_{22}^{\min} = 7\text{E}7$ N and $K_{44}^{\min} = 8\text{E}11$ Nmm^2

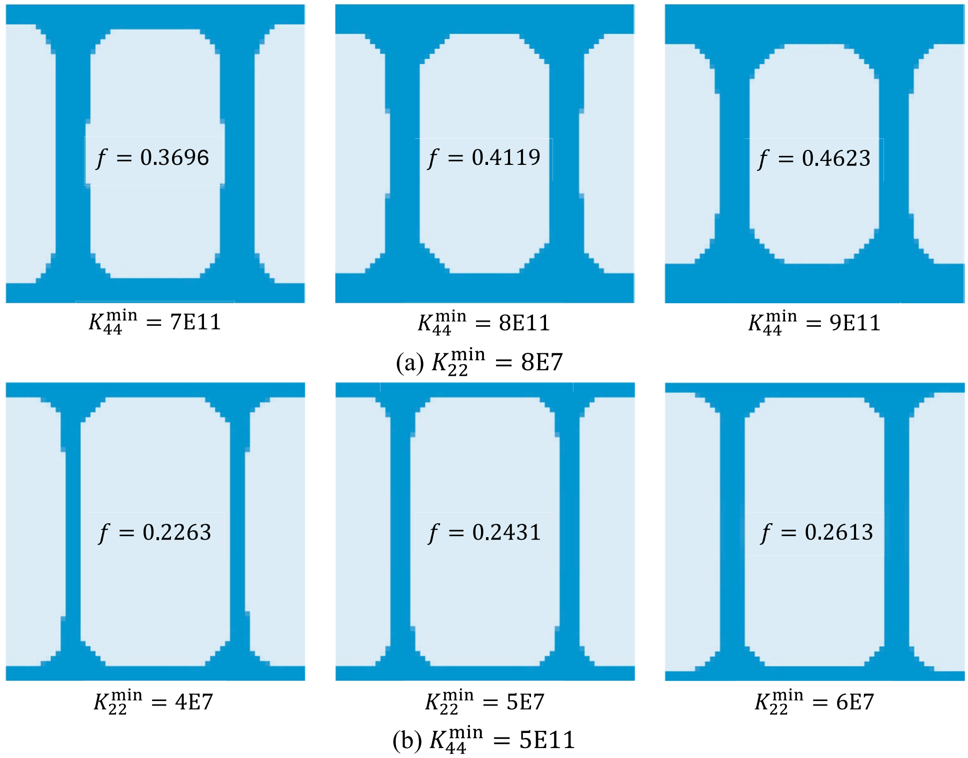

Fig. 6 Optimization results obtained with different bending and shear stiffness constraints, square domain; unit for K_{22}^{min} : N; for K_{44}^{min}: Nmm^2.

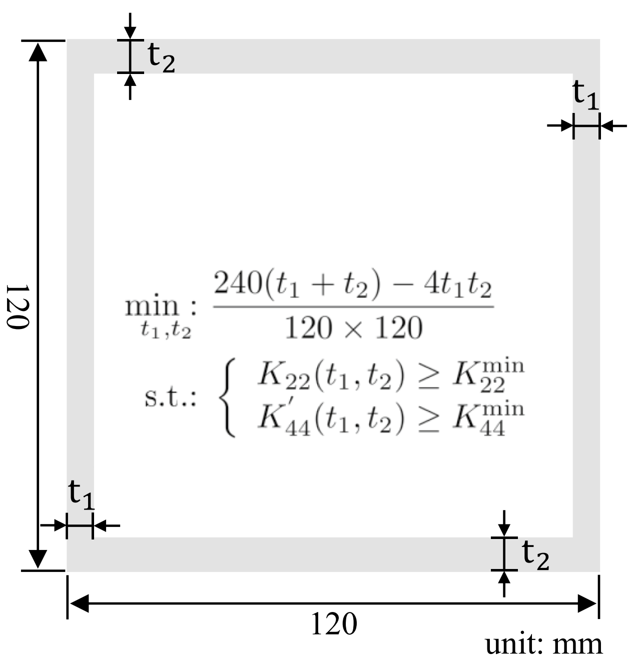

Fig. 7 Box beam geometry

equal to their respective minimum values. As expected, an increase in the minimum bending stiffness leads to a design with more material at the top and bottom of the cross section, whereas increasing the minimum shear stiffness results in thicker webs. For comparison, the same

Table 2 Optimal box beams compared with the topology optimization results

Constraints		Box beam			Topology
K_{22}^{min}/N	K_{44}^{min}/(Nmm^2)	t_1/mm	t_2/mm	f	f
8E7	7E11	15.538	10.290	0.3860	0.3696
8E7	8E11	15.507	13.790	0.4289	0.4119
8E7	9E11	15.430	17.928	0.4791	0.4623
4E7	5E11	7.615	7.445	0.2352	0.2263
5E7	5E11	9.68	6.736	0.2554	0.2431
4E7	5E11	11.682	6.01	0.2753	0.2613

optimization was performed over a 120 mm × 120 mm box beam cross section, with the thickness of the vertical and horizontal plates, t_1 and t_2, taken as variables, cfr. Fig. 7. Table 2 compares the box beam optimal results with those of Fig. 6, and highlights how, even for a simple problem like this, the topology optimization leads to a result that is marginally lighter than what achievable with a standard box cross section.

4.2 Shear, bending, and torsional stiffness constraints

Beyond the shear and bending stiffness, structural beams also require sufficient stiffness to resist twisting deformation.

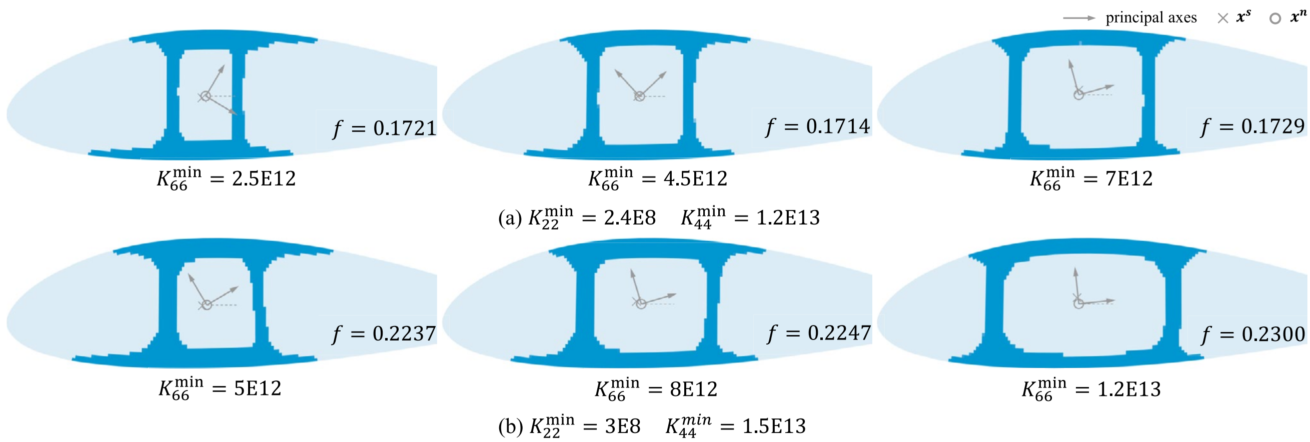

Fig. 8 Profile domain optimization results with different setting of minimum bending stiffness values; unit for $K_{22}^{\min}$: N; for $K_{44}^{\min}$ and $K_{66}^{\min}$: Nmm^2.

This subsection illustrates the influence of the torsional stiffness constraint on the cross-section topology. Since torsional stiffness is of paramount importance for slender structures like wings or wind turbine blades, we consider here the fx83w227-il profile domain. Due to the asymmetry of the profile design domain, the position of shear and normal stress centers will continually change during the optimization, while they barely move in the square domain case of Sec. 4.1. Thus, the bending and torsional stiffness from the decoupled matrix $\boldsymbol{K}'$ of Eq. (32) are used to define the constraints, giving rise to an optimization problem formulated as

$$\begin{cases} \underset{\rho}{\text{minimize}} \;\; f(\bar{\boldsymbol{\rho}}) \\ \text{subject to} \;\; K_{22}^{\min} - K_{22}(\bar{\boldsymbol{\rho}}) \leq 0, \\ \qquad\qquad\;\; K_{44}^{\min} - K_{44}'(\bar{\boldsymbol{\rho}}) \leq 0, \\ \qquad\qquad\;\; K_{66}^{\min} - K_{66}'(\bar{\boldsymbol{\rho}}) \leq 0, \\ \qquad\qquad\;\; 0 \leq \rho_i \leq 1 \end{cases}$$

Two sets of optimization results are illustrated in Fig. 8. The first set (Fig. 8a) comprises three results obtained with different minimum torsional stiffness $K_{66}^{\min}$, but constant minimum shear and bending stiffness, setting $K_{22}^{\min} = 2.4\text{E}8$ N and $K_{44}^{\min} = 1.2\text{E}13\,\text{Nmm}^2$. The comparison reveals that a higher required torsional stiffness has only a light impact on the area ratio of the cross section, given the current minimum stiffness constraints for shear and bending. This is because the code determines the optimal cross section by adjusting the material distribution, according to the required minimum stiffness. To increase torsional stiffness, the distance between the webs is enlarged, resulting in a greater closed-cell area and, consequently, enhanced torsional rigidity. The same trend is obtained with the results of Fig. 8b, in which the minimum shear and bending stiffness values are defined as $K_{22}^{\min} = 3\text{E}8$ N and $K_{44}^{\min} = 1.5\text{E}13\,\text{Nmm}^2$, respectively.

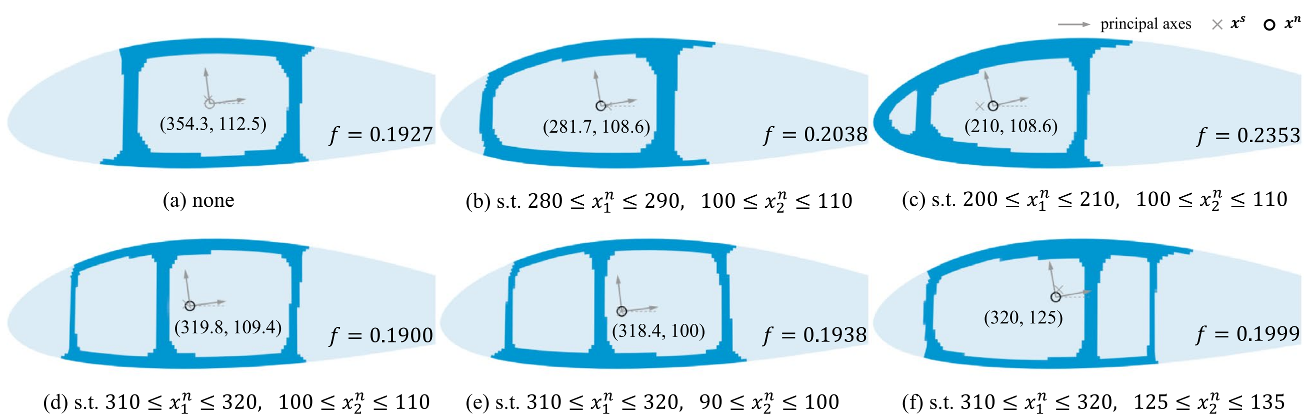

Fig. 9 Profile domain optimization results with different constraints on the position of $\boldsymbol{x}^n$, but with the same $K_{22}^{\min} = 2.5\text{E}8$ N, $K_{44}^{\min} = 1.3\text{E}13\,\text{Nmm}^2$, and $K_{66}^{\min} = 1\text{E}13\,\text{Nmm}^2$; unit of $\boldsymbol{x}^n$: mm

4.3 The effect of the constraints on the position of centers and on the orientation of principal axis

The objective of this subsection is to demonstrate the effectiveness of the proposed optimization framework when the position of the normal stress center $\boldsymbol{x}^n$, shear center $\boldsymbol{x}^s$, and the rotation angle of principal axis ϕ^p are controlled by imposing specified upper and lower limits. Figure 9 demonstrates the results obtained with different constraints on the position of the normal stress center, all with the minimum stiffness constraint values set as $K_{22}^{\min} = 2.5\text{E}8$ N, $K_{44}^{\min} = 1.3\text{E}13\,\text{Nmm}^2$ and $K_{66}^{\min} = 1\text{E}13\,\text{Nmm}^2$. All the optimized cross sections, whose position of $\boldsymbol{x}^n$ is shown in the figure, have stiffness values equal to the minimum setting. As a baseline, Fig. 9a presents the optimal cross section obtained without the imposition of constraints on $\boldsymbol{x}^n$, which results in $\boldsymbol{x}^n = (354.3, 112.5)$ mm. The optimized cross sections in Fig. 9b and c are obtained by imposing the same constraint for x_2^n ($100\,\text{mm} \le x_2^n \le 110\,\text{mm}$), but with different constraints on x_1^n, namely $280\,\text{mm} \le x_1^n \le 290\,\text{mm}$ and $200\,\text{mm} \le x_1^n \le 210\,\text{mm}$. Similarly, results of Fig. 9d to e share the same constraint on x_1^n, with $310\,\text{mm} \le x_1^n \le 320\,\text{mm}$, but have different allowable ranges for x_2^n. It is interesting to note that, keeping the position of $\boldsymbol{x}^n$ strictly within the specified range, the associated constraints can affect not only the final value of the objective function, but also the topology of the cross section, potentially altering it from a single-cell to a two-cell design.

Figure 10 shows the results obtained by constraining also the position of shear center $\boldsymbol{x}^s$, which thus introduces four additional constraints, bringing the total to eleven. The baseline result of Fig. 10a is derived by imposing minimum stiffness constraints ($K_{22}^{\min} = 2.5\text{E}8$ N, $K_{44}^{\min} = 1.3\text{E}13\,\text{Nmm}^2$, and $K_{66}^{\min} = 1\text{E}13\,\text{Nmm}^2$) and only limiting the position of $\boldsymbol{x}^n$ as $320\,\text{mm} \le x_1^n \le 330\,\text{mm}$ and $100\,\text{mm} \le x_2^n \le 110\,\text{mm}$; the shear center of the optimized design is at $\boldsymbol{x}^s = (319.4, 112.2)$ mm. The designs of Fig. 10b and c are obtained by adding different constraints on the position of $\boldsymbol{x}^s$, which in both cases lies within the prescribed region. Furthermore, Fig. 10d illustrates the case where the admissible region for two centers is shifted to left. Overall, it can be observed that, in most cases, the two centers are located close to each other. However, they can be separated by applying reasonable constraints. Figure 10e and f show two cases in which the admissible regions for the centers differ markedly. The resulting cross sections exhibit centers that are widely separated, prompting the optimizer toward different topology of the cross sections.

From the results above, it can be observed that the orientation of the principal axes varies across the different cases; this variation can be controlled by activating the related constraints. Figure 11 presents the results obtained under different constraints on the rotation angle of principal axis ϕ^p, and on bending stiffness about different axis.

In this group, the constraints for the stiffness values are set as $K_{22}^{\min} = 2.5\text{E}8$ N, $K_{44}^{\min} = 1.35\text{E}13\,\text{Nmm}^2$, and $K_{66}^{\min} = 1.2\text{E}13\,\text{Nmm}^2$, while the constraints for the $\boldsymbol{x}^n$ are defined as $300\,\text{mm} \le x_1^n \le 310\,\text{mm}$, and $100\,\text{mm} \le x_2^n \le 110\,\text{mm}$. The derived results are presented along with the rotation angle ϕ^p, as well as the bending stiffness value $K_{44}^{'}$ and K_{44}^{p}, which are the values in the original reference system and the principal axis system, respectively. In the first three cases (a) to (c), the bending stiffness constraint is applied to $K_{44}^{'}$. The baseline case, without any constraint for the value of ϕ^p, is shown in the Fig. 11a, with a resulting $\phi^p = 6.15°$. The bending stiffness in the original

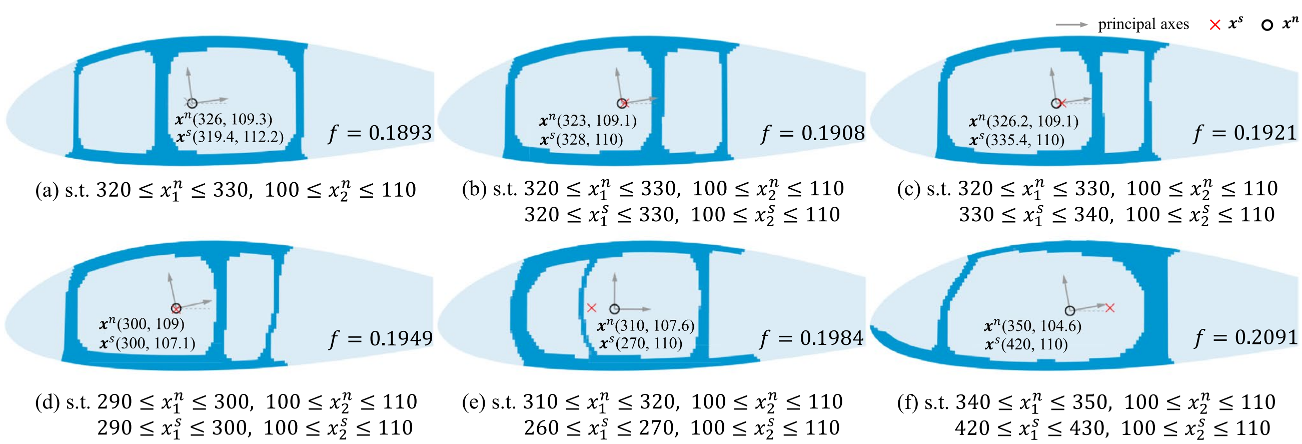

Fig. 10 Profile domain optimization results with different constraints on the position of $\boldsymbol{x}^s$ and $\boldsymbol{x}^n$, but with the same $K_{22}^{\min} = 2.5\text{E}8$ N, $K_{44}^{\min} = 1.3\text{E}13\,\text{Nmm}^2$, and $K_{66}^{\min} = 1\text{E}13\,\text{Nmm}^2$; unit of $\boldsymbol{x}^n$ and $\boldsymbol{x}^s$: mm

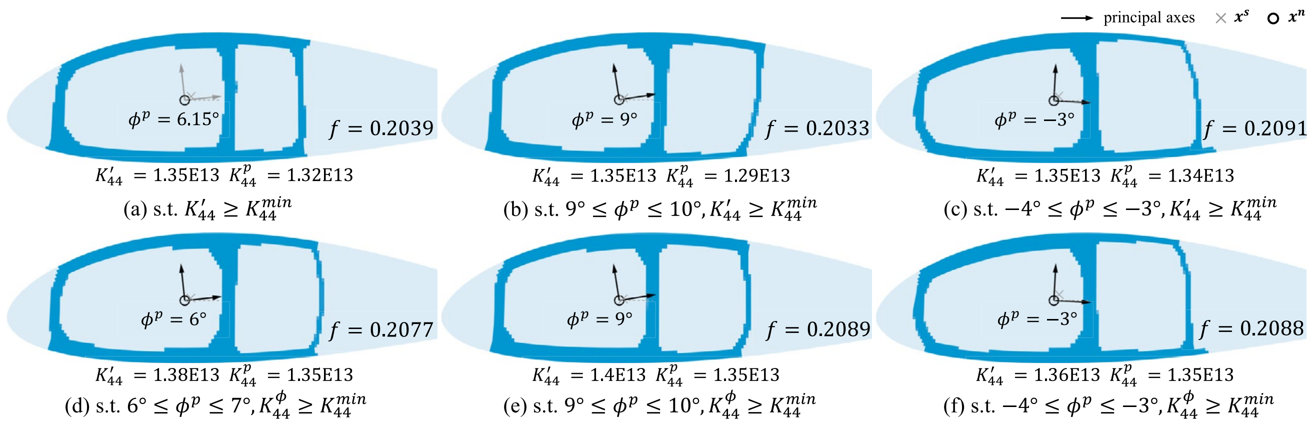

Fig. 11 Profile domain optimization results with different constraints on the rotation angle ϕ^p and bending stiffness, but with the same $K^{\min}_{22} = 2.5\text{E}8$ N, $K^{\min}_{44} = 1.35\text{E}13$ Nmm^2, $K^{\min}_{66} = 1.2\text{E}13$ Nmm^2, $300\,\text{mm} \leq x^n_1 \leq 310\,\text{mm}$, and $100\,\text{mm} \leq x^n_2 \leq 110\,\text{mm}$

reference system is $K'_{44} = 1.35\text{E}13$ Nmm^2, equal to $K^{\min}_{44}$, whereas in the principal axis system, it is slightly lower, with $K^p_{44} = 1.32\text{E}13$ Nmm^2. For comparison, the results shown in Fig. 11b and c are obtained with the rotation angle ϕ^p restricted in the prescribed range, demonstrating the effectiveness of corresponding constraints.

Above all, it can be seen that, if the bending stiffness constraint is applied to K'_{44}, the resulting bending stiffness in principal axis system, K^p_{44}, is slightly smaller. However, imposing a direct constraint on K^p_{44}, which depends on ϕ^p, would result in a highly nonlinear constraint. Instead, one can constrain the bending stiffness with respect to reference system rotated by $\phi = (\phi^{\min} + \phi^{\max})/2$. This leads to the constraint $K^\phi_{44} \geq K^{\min}_{44}$, so that at convergence, i.e., when ϕ^p would have been brought within the tight bound $\phi^{\min} \leq \phi^p \leq \phi^{\max}$, the resulting K^ϕ_{44} would be closer to the actual K^p_{44}.

Figure 11d to f present the optimal results obtained with constraints not only on ϕ^p, but also on the bending stiffness K^ϕ_{44}. From the results it can be seen that the sought rotation angle ϕ^p is achieved, with the resulting bending stiffness in the actual principal axis system K^p_{44} close to $K^{\min}_{44}$.

4.4 Stress constraint

The aim of this subsection is to verify the effectiveness of the stress constraint within the proposed optimization framework. This allows to account not only for stiffness requirements, but also for the strength one. In order to avoid coupling terms in the stiffness matrix $\boldsymbol{K}$, we consider here the stress caused by the bending moment m_1 and torsional moment m_3.

The baseline design of Fig. 12a is obtained by imposing only stiffness constraints ($K^{\min}_{22} = 2.5\text{E}8$ N, $K^{\min}_{44} = 1.25\text{E}13$ Nmm^2, and $K^{\min}_{66} = 8\text{E}12$ Nmm^2). With an allowable stress of $\sigma_{\text{allow}} = 200$ MPa, a combination of bending and torsional moments ($m_1 = 3.24\text{E}8$ Nmm, $m_3 = 7.2\text{E}7$ Nmm) brings the maximum von Mises stress above the limit. After enforcing the stress constraint, the maximum von Mises stress is reduced to the allowable stress under the same applied moments, as shown in Fig. 12b. However, this leads to the stiffness K'_{44} and K'_{66} exceeding their respective minimum values, with $K'_{44} = 1.33\text{E}13$ Nmm$^2 > K^{\min}_{44}$ and $K'_{66} = 8.53\text{E}12$ Nmm$^2 > K^{\min}_{66}$. Consequently, the objective function is increased by about 6%, highlighting that additional material is required to keep the maximum von Mises stress below the admissible limit.

An additional set of results, obtained with different combinations of bending and torsional moments, and with $\sigma_{\text{allow}} = 200$ MPa, $K^{\min}_{22} = 2.5\text{E}8$ N, $K^{\min}_{44} = 1.25\text{E}13$ Nmm^2, and $K^{\min}_{66} = 8\text{E}12$ Nmm^2, are illustrated in Fig. 13. Specifically, Fig. 13a shows the optimized configuration result by only applying the bending moment $m_1 = 3.6\text{E}8$ Nmm, leading to a bending stiffness $K'_{44} = 1.43\text{E}13$ Nmm^2 that is greater than $K^{\min}_{44}$. If the moments transmitted by the cross sections are equal to $m_1 = 2.88\text{E}8$ Nmm and $m_3 = 7.2\text{E}7$ Nmm, the resulting design, as shown in Fig. 13b, is characterized by an inactive stress constraint, $\bar{\sigma}_{PN} < \sigma_{\text{allow}}$, with an objective function $f = 0.1833$ almost equal to that obtained without imposing any strength constraints, $f = 0.1819$. Finally, the design of Fig. 13c, obtained with the higher moments $m_1 = 2.88\text{E}8$ Nmm and $m_3 = 1.08\text{E}8$ Nmm, satisfies the strength constraint, but has both K'_{44} and K'_{66} exceeding minimum stiffness values, leaving these two constraints inactive.

The results in Fig. 14 examine how different allowable stress values affect the optimal design. In this study, the stiffness requirement is set as $K^{\min}_{22} = 2.5\text{E}8$ N,

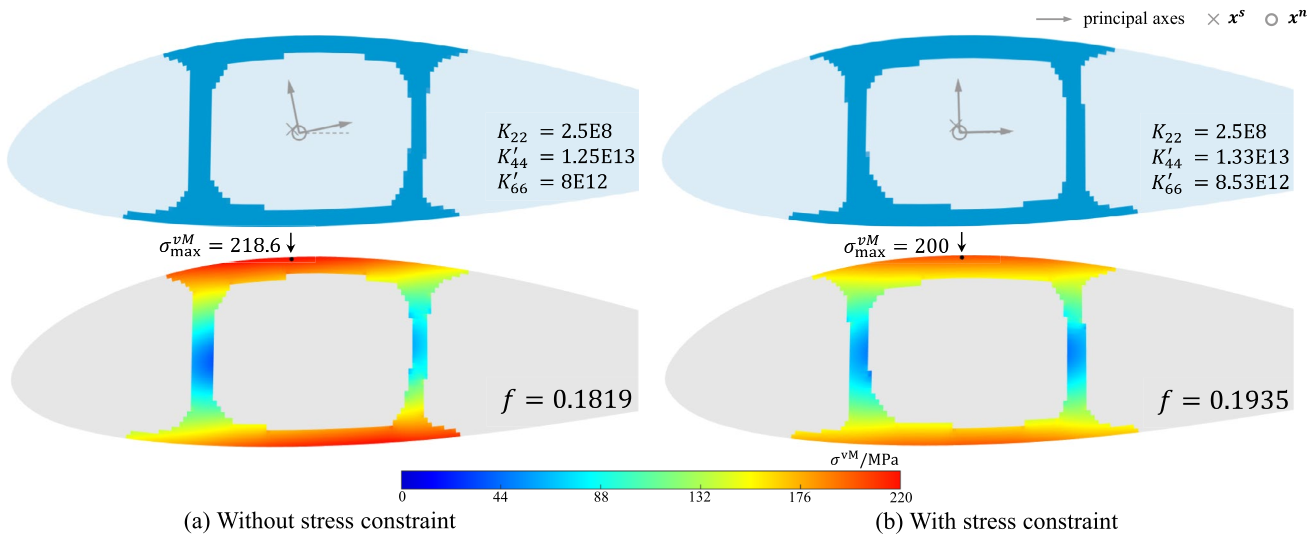

Fig. 12 The effect of stress constraints with minimum stiffness set as $K_{22}^{min} = 2.5E8$ N, $K_{44}^{min} = 1.25E13\,\text{Nmm}^2$, and $K_{66}^{min} = 8E12\,\text{Nmm}^2$, under the moments $m_1 = 3.24E8$ Nmm, $m_3 = 7.2E7$ Nmm, and with $\sigma_{max} = 200$ MPa; top: topology; bottom: vM stress contour

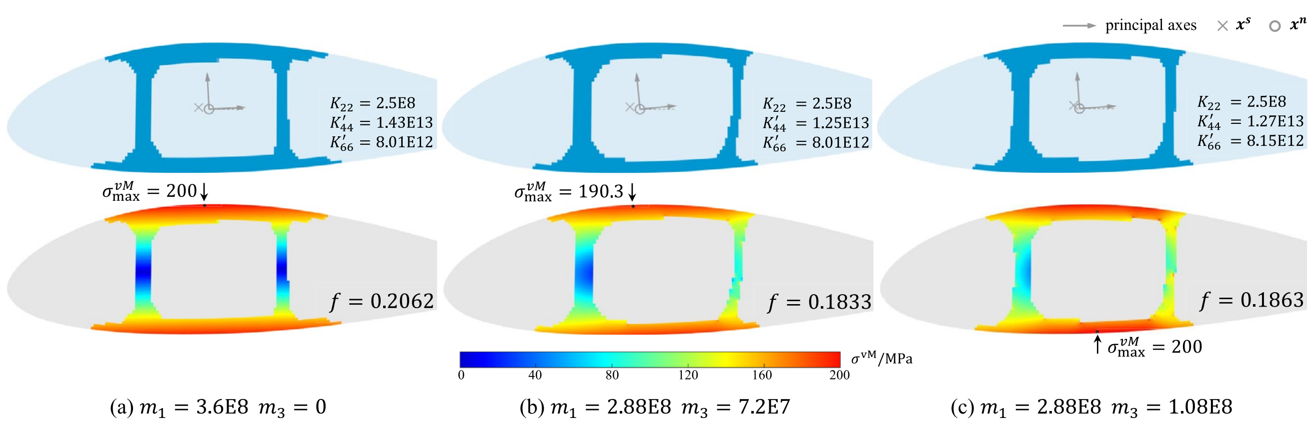

Fig. 13 Stress-constrained designs obtained with different combination of m_1 and m_3; $K_{22}^{min} = 2.5E8$ N, $K_{44}^{min} = 1.25E13\,\text{Nmm}^2$, and $K_{66}^{min} = 8E12\,\text{Nmm}^2$; top: topology; bottom: vM stress contour; unit of m_1 and m_3: Nmm

$K_{44}^{min} = 1.35E13\,\text{Nmm}^2$, and $K_{66}^{min} = 1.1E13\,\text{Nmm}^2$, while the applied bending moment are $m_1 = 3.24E8$ Nmm and $m_3 = 1.08E8$ Nmm, respectively. Figure 14b shows the result for $\sigma_{allow} = 200$ MPa, leading to a bending stiffness $K'_{44} = 1.3547E13\,\text{Nmm}^2$, slightly above the minimum, while the maximum von Mises stress reaches the limit of 200 MPa. The reduced allowable stress of 190 MPa yields the cross section shown in Fig 14a. In comparison with Fig. 14b, the objective function rises to 0.2115, accompanied by a higher bending stiffness of $K'_{44} = 1.43E13\,\text{Nmm}^2$, and torsional stiffness of $K'_{66} = 1.17E13\,\text{Nmm}^2$. The increase occurs because the maximum stress on the cross section must be below the σ_{allow}, which requires additional material to prevent the stress level from exceeding the admissible limit. If, instead, the allowable stress is set to the higher value of 210 MPa, the resulting cross section shows nearly the same area proportion as the case of Fig 14b, while the maximum stress is equal to 200.9 MPa, suggesting that the higher stress limit renders the stress constraints inactive, offering a wider design space.

4.5 Implementation of all the constraints

Following the verification about the influence of different constraints on the topology optimization procedure in previous subsections, this subsection presents optimization results with the imposition all the different types of constraints

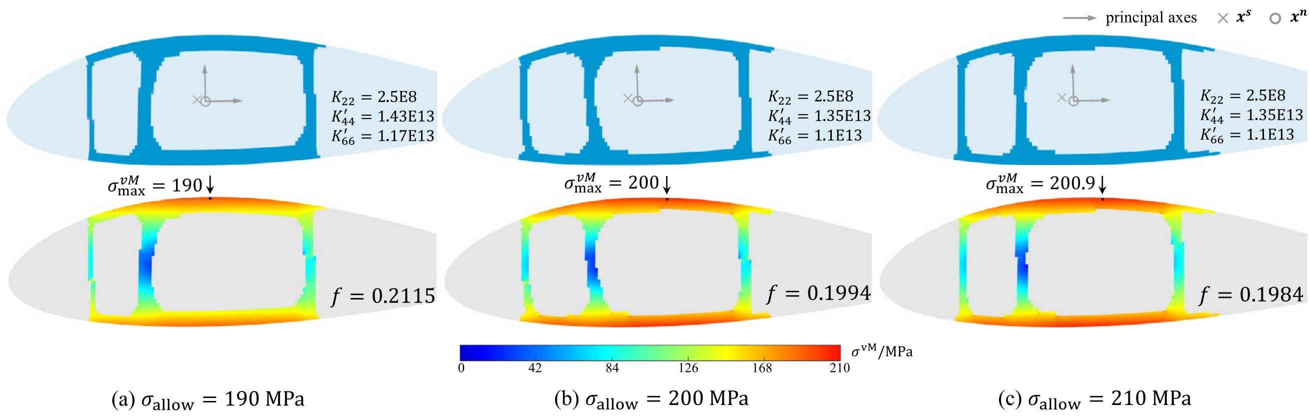

Fig. 14 Stress-constrained designs obtained with different allowable stress σ_{allow}; $K_{22}^{\min} = 2.5\text{E}8$ N, $K_{44}^{\min} = 1.35\text{E}13\,\text{Nmm}^2$, and $K_{66}^{\min} = 1.1\text{E}13\,\text{Nmm}^2$, under the moments $m_1 = 3.24\text{E}8$ Nmm, $m_3 = 1.08\text{E}8$ Nmm; top: topology; bottom: vM stress contour

simultaneously. The optimization problem, with a total of fourteen constraints, is thus formulated as

$$\begin{cases} \underset{\rho}{\text{minimize}}\ f(\bar{\rho}) \\ \text{subject to}\ K_{22}^{\min} - K_{22}(\bar{\rho}) \le 0, \\ \qquad K_{44}^{\min} - K_{44}^{\phi}(\bar{\rho}) \le 0, \\ \qquad K_{66}^{\min} - K'_{66}(\bar{\rho}) \le 0, \\ \qquad (x_1^{n\,\min}, x_2^{n\,\min}) \le (x_1^n, x_2^n) \le (x_1^{n\,\max}, x_2^{n\,\max}), \\ \qquad (x_1^{s\,\min}, x_2^{s\,\min}) \le (x_1^s, x_2^s) \le (x_1^{s\,\max}, x_2^{s\,\max}), \\ \qquad \phi^{min} \le \phi^p \le \phi^{max} \\ \qquad \bar{\sigma}_{PN} - \sigma_{\text{allow}} \le 0, \\ \qquad 0 \le \rho_i \le 1. \end{cases} \tag{55}$$

Three examples are presented with different design constraint settings. The results are illustrated in Fig 15, while the exact constraint values and the corresponding optimization result data are summarized in Table 3.

In the first case, as Fig. 15a, the allowable stress is set as $\sigma_{\text{allow}} = 190$ MPa, while the range for rotation angle ϕ^p is constrained within $10° \le \phi^p \le 11°$. Applied moments lead to a cross section with objective function as 0.2245, bending stiffness values of $K'_{44} = 1.46\text{E}13\,\text{Nmm}^2$ and $K_{44}^p = 1.41\text{E}13\,\text{Nmm}^2$, both exceeding $K_{44}^{\min}$. The second optimal cross section, as shown in Fig 15b, has the stiffness values that are equal to the corresponding constraints values, with the resulting rotation angle $\phi^p = -5°$. Under the applied moments, the maximum von Mises stress among the evaluation points is equal to 185.9 MPa, far below from the allowable stress of $\sigma_{\text{allow}} = 200$ MPa. In the final example, the constraints ϕ^p ensures that the deviation of principal axis from the original system does not exceed 0.5°, while the resulting cross section successfully maintains the centers within the specified bounds, still satisfying the stiffness requirements, and limiting the maximum von Mises stress equal to the admissible value.

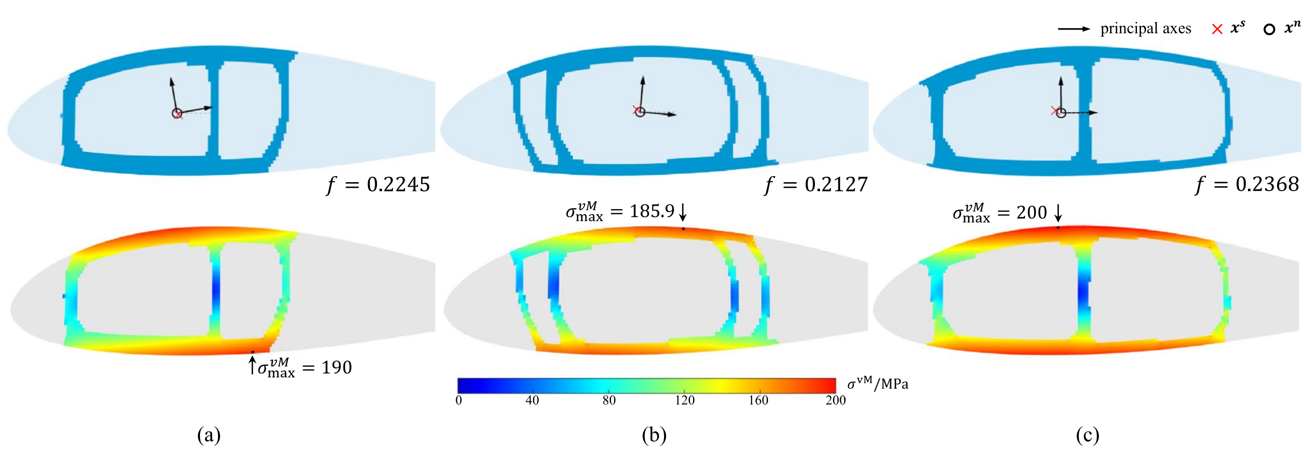

Fig. 15 Optimization results obtained with all the constraints imposed; top: topology; bottom: vM stress contour

Table 3 Constraints and corresponding optimization result data for the results of Fig. 15; unit of K_{22}: N, of K^p_{44}, K'_{44} and K'_{66}: Nmm^2, $\boldsymbol{x}^n$ and $\boldsymbol{x}^s$: mm, $m_{\{1,3\}}$: Nmm, vM stress: MPa

	Stiffness		Centers and angle		Maximum VM		
	Constraints	Value	Constraints	Value	Resultant and limit	Value	f
	$K^{min}_{22} = 2.5E8$	$K_{22} = 2.5E8$	$290 \le x^n_1 \le 300$	$\boldsymbol{x}^n(297.4, 108.9)$			
Fig. 15a	$K^{min}_{44} = 1.3E13$	$K'_{44} = 1.46E13$	$100 \le x^n_2 \le 110$		$\sigma_{allow} = 190$		
		$K^p_{44} = 1.41E13$	$290 \le x^s_1 \le 300$	$\boldsymbol{x}^s(300, 106.4)$	$m_1 = 3.24E8$	190	0.2245
	$K^{min}_{66} = 1.25E13$	$K'_{66} = 1.25E13$	$100 \le x^s_2 \le 110$		$m_3 = 1.08E8$		
			$10° \le \phi^p \le 11°$	$\phi^p = 10°$			
	$K^{min}_{22} = 2.5E8$	$K_{22} = 2.5E8$	$340 \le x^n_1 \le 350$	$\boldsymbol{x}^n(350, 111.1)$			
Fig. 15b	$K^{min}_{44} = 1.35E13$	$K'_{44} = 1.37E13$	$110 \le x^n_2 \le 120$		$\sigma_{allow} = 200$		
		$K^p_{44} = 1.35E13$	$340 \le x^s_1 \le 350$	$\boldsymbol{x}^s(344.6, 115.2)$	$m_1 = 2.88E8$	185.9	0.2127
	$K^{min}_{66} = 1.35E13$	$K'_{66} = 1.35E13$	$110 \le x^s_2 \le 120$		$m_3 = 1.08E8$		
			$-6° \le \phi^p \le -5°$	$\phi^p = -5°$			
	$K^{min}_{22} = 2.5E8$	$K_{22} = 2.5E8$	$320 \le x^n_1 \le 330$	$\boldsymbol{x}^n(330, 110.1)$			
Fig. 15c	$K^{min}_{44} = 1.5E13$	$K'_{44} = 1.56E13$	$110 \le x^n_2 \le 120$		$\sigma_{allow} = 200$		
		$K^p_{44} = 1.56E13$	$320 \le x^s_1 \le 330$	$\boldsymbol{x}^s(320.3, 114.5)$	$m_1 = 3.78E8$	200	0.2368
	$K^{min}_{66} = 1.5E13$	$K'_{66} = 1.5E13$	$110 \le x^s_2 \le 120$		$m_3 = 1.26E8$		
			$-0.5° \le \phi^p \le 0.5°$	$\phi^p = 0.5°$			

5 Conclusions

In this paper, we present a topology optimization framework for the design of isotropic beam cross sections, formulated using the SIMP method. The cross-section analysis is performed with the latest ANBA4 code. The 6×6 stiffness matrix and the stress evaluation are based on the central solutions from the differential equations system that is built on the cross section. Starting from an arbitrarily shaped design domain, the optimization method identifies the cross section with the minimum material usage, while ensuring the satisfaction of the prescribed design constraints. The first category of constraints encompasses shear, bending, and torsional stiffness, whereas the second category is defined by the admissible range for the position of normal stress and shear centers, and the orientation of principal axis. In addition, a global stress constraint is constructed with P-norm function, by incorporating the relaxed von Mises stress at all evaluation points. The adjoint method is adopted for the sensitivity analysis of the stiffness matrix and the global stress function.

Several groups of examples are presented to illustrate the impact of different constraints on the optimized cross-section topology. From the examples with different setting on minimum stiffness values, we can find that higher bending stiffness requirement allows more material being distributed at the top and bottom, whereas

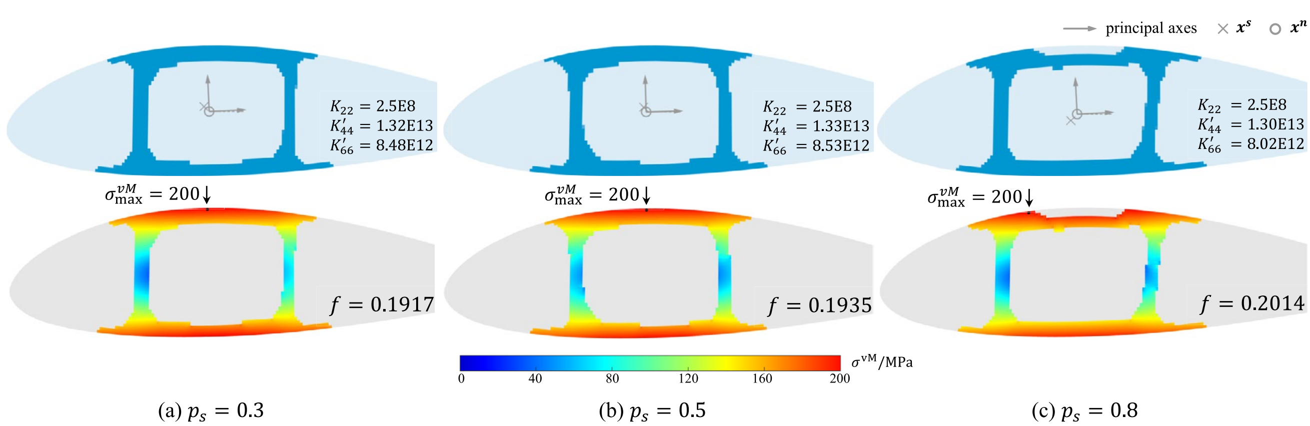

Fig. 16 Optimization results obtained with different values of the stress relaxation parameter p_s; top: topology; bottom: vM stress contour

increasing shear stiffness results in more material concentrated in the middle. Furthermore, a higher torsional stiffness requirement produces, under identical shear and bending stiffness constraints, a larger closed-cell area. These outcomes are consistent with analytical results, and confirm the soundness of the optimization procedure. Numerical results also demonstrate that constraints on the position of the normal stress center and shear center significantly influence the material distribution on the cross section. The orientation of principal axis can also be effectively controlled through the imposition of corresponding constraints. In such case, the bending stiffness can be evaluated about an arbitrary axis rotated from the original reference system. Finally, enforcing the stress constraint results in optimal cross sections on which the von Mises stress of each evaluation point does not exceed the allowable limit. Nevertheless, when the cross section is subjected to higher bending and torsional moments, the stress constraint may increase the required stiffness, potentially rendering some stiffness constraints inactive. The presented method can be potentially expanded to the cross-section optimization of realistic slender structures like, helicopter blade and wind turbine blade, combined with their real application cases.

Future research can be performed to extend the current framework to multi-scale topology optimization, enabling the simultaneous design of beam cross sections at both macro and micro scales. Furthermore, the incorporation of composite materials can be explored to facilitate the optimization design of composite beam cross sections with superior structural properties.

Appendix A The effect of the stress penalization factor

Consistently with other published papers, we set the stress penalization factor as $p_s = 0.5$ (cfr. Equation 39) in our study, since it provides a stable behavior during the optimization process. Figure 16 reports, for completeness, a set of results obtained with different values of p_s.

The baseline is the result of Fig. 12b in the manuscript, as shown here with $p_s = 0.5$. With $p_s = 0.3$ (result on the left), the objective function value is almost unchanged, with resulting stiffness coefficients K'_{22}, K'_{44}, and K'_{66} similar those obtained with $p_s = 0.5$. This suggests that $p_s = 0.3$ may be appropriate in certain cases; however, its suitability may not be generalized, as the stress distribution in lower-density elements could significantly affect the final outcome. On the other hand, the result on the right, obtained with $p_s = 0.8$, has a void at the top, where the maximum stress is expected, leading to a less efficient structure in bending and a larger objective function. Thus, big value of p_s do not seem to be a good choice. The value $p_s = 0.5$ suggested in the literature appears to be a good compromise.

Appendix B Adjoint derivation

In order to perform sensitivity analysis using the adjoint method, the 21 independent components of the stiffness matrix $\boldsymbol{K}$ are assembled in a vector, denoted as $\boldsymbol{K}_v$. This vectorization facilitates the construction of an augmented Lagrange systems that comprises 12 linear equation systems (four of which are trivial, namely $\boldsymbol{\Lambda}_7$, $\boldsymbol{\Lambda}_8$, $\boldsymbol{\Lambda}_9$, $\boldsymbol{\Lambda}_{10}$), each multiplied by a corresponding adjoint matrix λ_i. The resulting formulation is thus expressed as

$$\mathcal{L}(\overline{\rho}) = \boldsymbol{K}_v + \sum_{i=1}^{12} \lambda_i^T \boldsymbol{\Lambda}_i \tag{B1}$$

The set of 12 linear equation systems are summarized below:

$$\begin{cases} \boldsymbol{\Lambda}_1 = \boldsymbol{E}\boldsymbol{c}_{11} + \boldsymbol{H}\boldsymbol{c}_{10} = \boldsymbol{0} \\ \boldsymbol{\Lambda}_2 = \boldsymbol{E}\boldsymbol{c}_{21} + \boldsymbol{H}\boldsymbol{c}_{20} = \boldsymbol{0} \\ \boldsymbol{\Lambda}_3 = \boldsymbol{E}\boldsymbol{c}_{32}^0 - \boldsymbol{M}\boldsymbol{c}_{30} + \boldsymbol{H}\boldsymbol{c}_{31}^0 = \boldsymbol{0} \\ \boldsymbol{\Lambda}_4 = \boldsymbol{E}\boldsymbol{c}_{42}^0 - \boldsymbol{M}\boldsymbol{c}_{40} + \boldsymbol{H}\boldsymbol{c}_{41}^0 = \boldsymbol{0} \\ \boldsymbol{\Lambda}_5 = \boldsymbol{A}\boldsymbol{n}_1 - \boldsymbol{b}_1 = \boldsymbol{0} \\ \boldsymbol{\Lambda}_6 = \boldsymbol{A}\boldsymbol{n}_2 - \boldsymbol{b}_2 = \boldsymbol{0} \\ \boldsymbol{\Lambda}_7 = \boldsymbol{c}_{31} - \boldsymbol{c}_{31}^0 - [\, \boldsymbol{c}_{10} \;\; \boldsymbol{c}_{20} \,]\boldsymbol{n}_1 = \boldsymbol{0} \\ \boldsymbol{\Lambda}_8 = \boldsymbol{c}_{32} - \boldsymbol{c}_{32}^0 - [\, \boldsymbol{c}_{11} \;\; \boldsymbol{c}_{21} \,]\boldsymbol{n}_1 = \boldsymbol{0} \\ \boldsymbol{\Lambda}_9 = \boldsymbol{c}_{41} - \boldsymbol{c}_{41}^0 - [\, \boldsymbol{c}_{10} \;\; \boldsymbol{c}_{20} \,]\boldsymbol{n}_2 = \boldsymbol{0} \\ \boldsymbol{\Lambda}_{10} = \boldsymbol{c}_{42} - \boldsymbol{c}_{42}^0 - [\, \boldsymbol{c}_{11} \;\; \boldsymbol{c}_{21} \,]\boldsymbol{n}_2 = \boldsymbol{0} \\ \boldsymbol{\Lambda}_{11} = \boldsymbol{E}\boldsymbol{c}_{33} - \boldsymbol{M}\boldsymbol{c}_{31} + \boldsymbol{H}\boldsymbol{c}_{32} = \boldsymbol{0} \\ \boldsymbol{\Lambda}_{12} = \boldsymbol{E}\boldsymbol{c}_{43} - \boldsymbol{M}\boldsymbol{c}_{41} + \boldsymbol{H}\boldsymbol{c}_{42} = \boldsymbol{0} \end{cases} \tag{B2}$$

All the adjoint matrices λ_i will be derived by solving the following linear equation systems in sequence,

$$\begin{aligned} \frac{\partial \boldsymbol{K}_v}{\partial \boldsymbol{c}_{43}} + \lambda_{12}^T \frac{\partial \boldsymbol{\Lambda}_{12}}{\partial \boldsymbol{c}_{43}} &= \boldsymbol{0} \\ \frac{\partial \boldsymbol{K}_v}{\partial \boldsymbol{c}_{33}} + \lambda_{11}^T \frac{\partial \boldsymbol{\Lambda}_{11}}{\partial \boldsymbol{c}_{33}} &= \boldsymbol{0} \\ \frac{\partial \boldsymbol{K}_v}{\partial \boldsymbol{c}_{42}} + \lambda_{10}^T \frac{\partial \boldsymbol{\Lambda}_{10}}{\partial \boldsymbol{c}_{42}} + \lambda_{12}^T \frac{\partial \boldsymbol{\Lambda}_{12}}{\partial \boldsymbol{c}_{42}} &= \boldsymbol{0} \\ \frac{\partial \boldsymbol{K}_v}{\partial \boldsymbol{c}_{32}} + \lambda_{8}^T \frac{\partial \boldsymbol{\Lambda}_{8}}{\partial \boldsymbol{c}_{32}} + \lambda_{11}^T \frac{\partial \boldsymbol{\Lambda}_{11}}{\partial \boldsymbol{c}_{32}} &= \boldsymbol{0} \\ \frac{\partial \boldsymbol{K}_v}{\partial \boldsymbol{c}_{41}} + \lambda_{9}^T \frac{\partial \boldsymbol{\Lambda}_{9}}{\partial \boldsymbol{c}_{41}} + \lambda_{12}^T \frac{\partial \boldsymbol{\Lambda}_{12}}{\partial \boldsymbol{c}_{41}} &= \boldsymbol{0} \end{aligned}$$

$$\frac{\partial \boldsymbol{K}_v}{\partial \boldsymbol{c}_{31}} + \lambda_{7}^T \frac{\partial \boldsymbol{\Lambda}_{7}}{\partial \boldsymbol{c}_{31}} + \lambda_{11}^T \frac{\partial \boldsymbol{\Lambda}_{11}}{\partial \boldsymbol{c}_{31}} = \boldsymbol{0} \tag{B3}$$

$$\lambda_6^T \frac{\partial \mathbf{\Lambda}_6}{\partial \boldsymbol{n}_2} + \lambda_9^T \frac{\partial \mathbf{\Lambda}_9}{\partial \boldsymbol{n}_2} + \lambda_{10}^T \frac{\partial \mathbf{\Lambda}_{10}}{\partial \boldsymbol{n}_2} = \mathbf{0}$$
$$\lambda_5^T \frac{\partial \mathbf{\Lambda}_5}{\partial \boldsymbol{n}_1} + \lambda_7^T \frac{\partial \mathbf{\Lambda}_7}{\partial \boldsymbol{n}_1} + \lambda_8^T \frac{\partial \mathbf{\Lambda}_8}{\partial \boldsymbol{n}_1} = \mathbf{0}$$
$$\lambda_4^T \frac{\partial \mathbf{\Lambda}_4}{\partial \boldsymbol{c}_{42}^0} + \lambda_6^T \frac{\partial \mathbf{\Lambda}_6}{\partial \boldsymbol{c}_{42}^0} + \lambda_{10}^T \frac{\partial \mathbf{\Lambda}_{10}}{\partial \boldsymbol{c}_{42}^0} = \mathbf{0}$$
$$\lambda_3^T \frac{\partial \mathbf{\Lambda}_3}{\partial \boldsymbol{c}_{32}^0} + \lambda_5^T \frac{\partial \mathbf{\Lambda}_5}{\partial \boldsymbol{c}_{32}^0} + \lambda_8^T \frac{\partial \mathbf{\Lambda}_8}{\partial \boldsymbol{c}_{32}^0} = \mathbf{0}$$

$$\frac{\partial \boldsymbol{K}_v}{\partial \boldsymbol{c}_{21}} + \lambda_2^T \frac{\partial \mathbf{\Lambda}_2}{\partial \boldsymbol{c}_{21}} + \lambda_5^T \frac{\partial \mathbf{\Lambda}_5}{\partial \boldsymbol{c}_{21}} + \lambda_6^T \frac{\partial \mathbf{\Lambda}_6}{\partial \boldsymbol{c}_{21}} + \lambda_8^T \frac{\partial \mathbf{\Lambda}_8}{\partial \boldsymbol{c}_{21}} + \lambda_{10}^T \frac{\partial \mathbf{\Lambda}_{10}}{\partial \boldsymbol{c}_{21}} = \mathbf{0}$$

$$\frac{\partial \boldsymbol{K}_v}{\partial \boldsymbol{c}_{11}} + \lambda_1^T \frac{\partial \mathbf{\Lambda}_1}{\partial \boldsymbol{c}_{11}} + \lambda_5^T \frac{\partial \mathbf{\Lambda}_5}{\partial \boldsymbol{c}_{11}} + \lambda_6^T \frac{\partial \mathbf{\Lambda}_6}{\partial \boldsymbol{c}_{11}} + \lambda_8^T \frac{\partial \mathbf{\Lambda}_8}{\partial \boldsymbol{c}_{11}} + \lambda_{10}^T \frac{\partial \mathbf{\Lambda}_{10}}{\partial \boldsymbol{c}_{11}} = \mathbf{0}$$

In order to solve the first system, the following derivatives should be computed firstly

$$\begin{aligned}\frac{\partial \mathbf{\Lambda}_{12}}{\partial \boldsymbol{c}_{43}} &= \boldsymbol{E},\\ \frac{\partial \boldsymbol{K}}{\partial \boldsymbol{c}_{43}} &= \boldsymbol{T}^T \frac{\partial \boldsymbol{Q}_d}{\partial \boldsymbol{c}_{43}} \boldsymbol{G} - \boldsymbol{G}^T \frac{\partial \boldsymbol{Q}_d^T}{\partial \boldsymbol{c}_{43}} \boldsymbol{W} \boldsymbol{Q}_d \boldsymbol{G}\\ &\quad - \boldsymbol{G}^T \boldsymbol{Q}_d^T \boldsymbol{W} \frac{\partial \boldsymbol{Q}_d}{\partial \boldsymbol{c}_{43}} \boldsymbol{G} + \boldsymbol{G}^T \frac{\partial \boldsymbol{Q}_d^T}{\partial \boldsymbol{c}_{43}} \boldsymbol{T},\end{aligned} \tag{B4}$$

where again $\boldsymbol{T}$ is a short for $[\boldsymbol{L};\boldsymbol{R}]$, $\boldsymbol{W}$ is a short for $\begin{bmatrix} \boldsymbol{M} & \boldsymbol{C}^T \\ \boldsymbol{C} & \boldsymbol{E} \end{bmatrix}$. Matrix $\partial \boldsymbol{K}_v / \partial \boldsymbol{c}_{43}$ can be obtained from Eq. (B4) by extracting the sensitivity information related to the 21 independent components of matrix $\boldsymbol{K}$. It is thus clear that both λ_{12} and λ_{11} can be obtained by solving a linear system associated to matrix $\boldsymbol{E}$. After having computed λ_{11} and λ_{12}, one can compute the following four adjoint multipliers $\lambda_i (i = 7, 8, 9, 10)$ and then proceed solving for the remaining six ones to derive $\lambda_i (i = 6, 5, 4, 3, 2, 1)$. With 21 independent components defining the vectorized stiffness matrix $\boldsymbol{K}_v$, computing all the adjoint multipliers requires the solution of a constant number of linear systems, independent from the dimension of the unknown design vector $\bar{\boldsymbol{\rho}}$.

After having computed all the adjoint multipliers λ_i, the derivative of the vector $\boldsymbol{K}_v$ with respect to the design variable $\bar{\boldsymbol{\rho}}$ can be obtained as

$$\frac{\mathrm{d}\boldsymbol{K}_v}{\mathrm{d}\bar{\boldsymbol{\rho}}} = \frac{\mathrm{d}\mathcal{L}(\bar{\boldsymbol{\rho}})}{\mathrm{d}\bar{\boldsymbol{\rho}}} = \frac{\partial \boldsymbol{K}_v}{\partial \bar{\boldsymbol{\rho}}} + \sum_{i=1}^{12} \lambda_i^T \frac{\partial \mathbf{\Lambda}_i}{\partial \bar{\boldsymbol{\rho}}} \tag{B5}$$

where $\partial \boldsymbol{K}_v / \partial \bar{\boldsymbol{\rho}}$ and $\partial \mathbf{\Lambda}_i / \partial \bar{\boldsymbol{\rho}}$ represent the partial derivatives, which are computed with the assumption of constant generalized eigenvectors, and can be determined analytically. For example, in the partial derivative with respect to $\bar{\rho}_i$, the terms computed assuming constant generalized eigenvectors can be written as

$$\begin{aligned}\frac{\partial \boldsymbol{K}}{\partial \bar{\rho}_i}\Big|_{\boldsymbol{Q}_d} &= \frac{\partial \boldsymbol{T}^T}{\partial \bar{\rho}_i} \boldsymbol{Q}_d \boldsymbol{G} - \boldsymbol{G}^T \boldsymbol{Q}_d^T \frac{\partial \boldsymbol{W}}{\partial \bar{\rho}_i} \boldsymbol{Q}_d \boldsymbol{G} + \boldsymbol{G}^T \boldsymbol{Q}_d^T \frac{\partial \boldsymbol{T}}{\partial \bar{\rho}_i},\\ \frac{\partial \mathbf{\Lambda}_{12}}{\partial \bar{\rho}_i}\Big|_{\boldsymbol{Q}_d} &= \frac{\partial \boldsymbol{E}}{\partial \bar{\rho}_i} \boldsymbol{c}_{11} + \frac{\partial \boldsymbol{H}}{\partial \bar{\rho}_i} \boldsymbol{c}_{10},\end{aligned} \tag{B6}$$

where the notation $|_{\boldsymbol{Q}_d}$ means that the derivative is independent of the generalized eigenvectors and

$$\frac{\partial \boldsymbol{W}}{\partial \bar{\rho}_i} = p(1-\rho_{\min})\bar{\rho}_i^{p-1} \begin{bmatrix} \boldsymbol{M}_i & \boldsymbol{C}_i^T \\ \boldsymbol{C}_i & \boldsymbol{E}_i \end{bmatrix}, \tag{B7}$$

$$\frac{\partial \boldsymbol{T}}{\partial \bar{\rho}_i} = p(1-\rho_{\min})\bar{\rho}_i^{p-1} \begin{bmatrix} \boldsymbol{L}_i \\ \boldsymbol{R}_i \end{bmatrix} \tag{B8}$$

The sensitivity analysis of the global stress function $\bar{\sigma}_{PN}$ can also be carried out using the adjoint method, but requires the inclusion of an additional constraint $\mathbf{\Lambda}_{13}$ that is given by

$$\mathbf{\Lambda}_{13} = \begin{bmatrix} \boldsymbol{L}^T & \boldsymbol{R}^T \end{bmatrix} \boldsymbol{Q}_d \boldsymbol{k}_d - \boldsymbol{\theta} = \mathbf{0}. \tag{B9}$$

The augmented scalar Lagrangian $\mathcal{L}^s(\bar{\boldsymbol{\rho}})$, built for the global stress function, is thus equal to

$$\mathcal{L}^s(\bar{\boldsymbol{\rho}}) = \sigma_{PN} + \sum_{i=1}^{13} \lambda_i^{sT} \mathbf{\Lambda}_i. \tag{B10}$$

The procedure that needs to be followed in order to compute the adjoint vectors λ_i^s is similar to that of the stiffness matrix $\boldsymbol{K}$, so there is no need to detail it here. After having computed the adjoint vectors λ_i^s, the gradient of the stress function σ_{PN} reads

$$\frac{\mathrm{d}\sigma_{PN}}{\mathrm{d}\bar{\boldsymbol{\rho}}} = \frac{\mathrm{d}\mathcal{L}^s(\bar{\boldsymbol{\rho}})}{\mathrm{d}\bar{\boldsymbol{\rho}}} = \frac{\partial \sigma_{PN}}{\partial \bar{\boldsymbol{\rho}}} + \sum_{i=1}^{13} \lambda_i^{sT} \frac{\partial \mathbf{\Lambda}_i}{\partial \bar{\boldsymbol{\rho}}}, \tag{B11}$$

where $\partial \sigma_{PN} / \partial \bar{\boldsymbol{\rho}}$ represents the partial derivative assuming constant $\boldsymbol{Q}_d$, and each component can be computed through

$$\frac{\partial \sigma_{PN}}{\partial \bar{\rho}_i}\Big|_{\boldsymbol{Q}_d} = \frac{\partial \sigma_{PN}}{\partial \hat{\sigma}_i^{vM}} \frac{\partial \hat{\sigma}_i^{vM}}{\partial \hat{\boldsymbol{\sigma}}_i} p^s \bar{\rho}_i^{p^s-1} \boldsymbol{D}\boldsymbol{B}\boldsymbol{P}_i \boldsymbol{Q}_d \boldsymbol{k}_d, \tag{B12}$$

$$\frac{\partial \sigma_{PN}}{\partial \hat{\sigma}_i^{vM}} = \frac{1}{p_N} \left(\sum_{k=1}^{N_e} \left(\hat{\sigma}_k^{vM}\right)^{p_N} \right)^{\frac{1}{p_N}-1} \cdot p_N \cdot \left(\hat{\sigma}_i^{vM}\right)^{p_N-1}, \tag{B13}$$

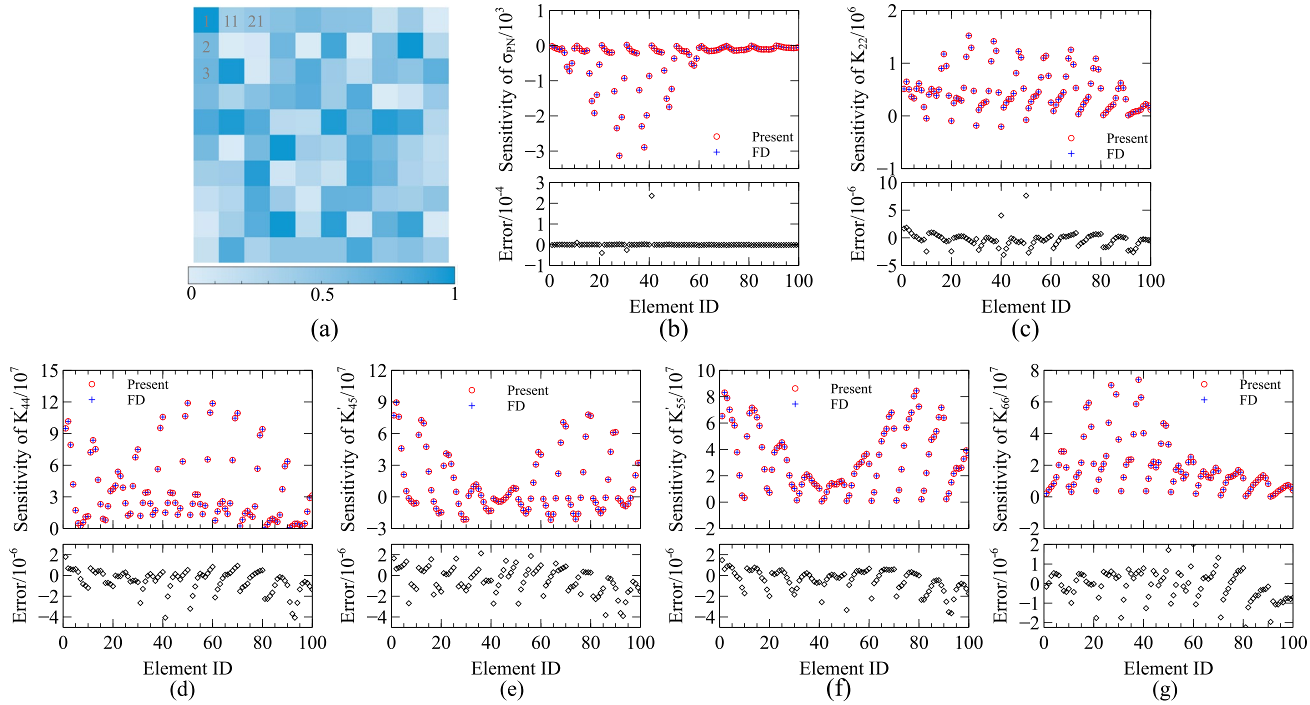

Fig. 17 Finite difference validation of the sensitivity information; relative errors computed with respect to the FD values

$$\frac{\partial \hat{\sigma}_i^{vM}}{\partial \hat{\boldsymbol{\sigma}}_i} = \frac{\hat{\boldsymbol{\sigma}}_i^T \cdot \boldsymbol{V}}{\hat{\sigma}_i^{vM}}, \tag{B14}$$

with matrix $\boldsymbol{V}$ defined by Eq. (41). The derivative of the generalized eigenvectors is accounted for by the terms $\lambda_i^{sT} \frac{\partial \boldsymbol{\Lambda}_i}{\partial \bar{\rho}}$ of Eq. (B11), similarly to the derivation of $\frac{\mathrm{d}\boldsymbol{K}_v}{\mathrm{d}\bar{\rho}}$ in Eqs. (B5, B6).

Appendix C Sensitivity validation

In order to validate the sensitivity information obtained using the adjoint method, a comparison is conducted with the results computed via finite difference method (FD). Since all the constraint derivatives are determined from $\mathrm{d}\boldsymbol{K}_v/\mathrm{d}\boldsymbol{\rho}$ and $\mathrm{d}\boldsymbol{\sigma}_{\mathrm{PN}}/\mathrm{d}\boldsymbol{\rho}$, this study only focuses on comparing the sensitivity of key stiffness values and global stress function with those obtained from the FD method.

The comparison considers a square domain of dimensions 20×20 mm, discretized into 100 elements, with the design variables randomly generated, as shown in Fig. 17a.

Bending and torsion moments of 6E4 Nmm are applied on the cross section. Material properties and all other parameters are consistent with those used in the previous examples. In the FD method, the increment for the design variable is set to $1\mathrm{E}-6$. Figure 17b compares the sensitivity value of the global stress function σ_{PN}, while Figure 17c to g compare the sensitivity of K_{22}, K_{44}', K_{45}', K_{55}', and K_{66}', respectively. The relative errors are computed with respect to the FD values. The comparison shows an excellent agreement, demonstrating the accuracy and validity of the adjoint method derivation.

Acknowledgements The support and funding provided by the China Scholarship Council (CSC) are acknowledged (CSC grant No. 202106260018).

Author contributions Zaiwei Lin contributed toward writing, visualization, investigation, data curation, and methodology. Marco Morandini contributed toward writing, supervision, investigation, conceptualization, and methodology.

Funding Open access funding provided by Politecnico di Milano within the CRUI-CARE Agreement. The first author's work was funded by the China Scholarship Council (CSC) (CSC grant No. 202106260018).

Data availability All data involved are included in the paper.

Declarations

Conflict of interest The authors declare that they have no conflict of interest.

Replication of results Sufficient information is provided throughout the paper to reproduce the results. We will provide further help if readers need it.

Open Access This article is licensed under a Creative Commons Attribution 4.0 International License, which permits use, sharing, adaptation, distribution and reproduction in any medium or format, as long as you give appropriate credit to the original author(s) and the source, provide a link to the Creative Commons licence, and indicate if changes were made. The images or other third party material in this article are included in the article's Creative Commons licence, unless indicated otherwise in a credit line to the material. If material is not included in the article's Creative Commons licence and your intended use is not permitted by statutory regulation or exceeds the permitted use, you will need to obtain permission directly from the copyright holder. To view a copy of this licence, visit http://creativecommons.org/licenses/by/4.0/.

References

Amir E, Amir O (2023) Free form shape optimization of three dimensional beams using cross section analysis. Int J Solids Struct 277–278(112):331. https://doi.org/10.1016/j.ijsolstr.2023.112331

Bendsøe MP (1989) Optimal shape design as a material distribution problem. Struct Optim 1(4):193–202. https://doi.org/10.1007/BF01650949

Bendsoe MP, Sigmund O (2013) Topology optimization: theory, methods, and applications. Springer, New York

Blasques JP (2014) Multi-material topology optimization of laminated composite beams with eigenfrequency constraints. Compos Struct 111:45–55. https://doi.org/10.1016/j.compstruct.2013.12.021

Blasques JP, Stolpe M (2012) Multi-material topology optimization of laminated composite beam cross sections. Compos Struct 94(11):3278–3289. https://doi.org/10.1016/j.compstruct.2012.05.002

Bruggi M (2008) On an alternative approach to stress constraints relaxation in topology optimization. Struct Multidiscip Optim 36(2):125–141. https://doi.org/10.1007/s00158-007-0203-6

Callejo A, Bauchau OA, Diskin B (2019) Adjoint method for the sensitivity analysis of composite beam cross-sections. Comput Struct 213:100–111. https://doi.org/10.1016/j.compstruc.2018.12.004

Cesnik CES, Hodges DH (1997) Vabs: a new concept for composite rotor blade cross-sectional modeling. J Am Helicopter Soc 42(1):27–38. https://doi.org/10.4050/JAHS.42.27

Cheng GD, Guo X (1997) ε-relaxed approach in structural topology optimization. Struct Optim 13(4):258–266. https://doi.org/10.1007/BF01197454

Díaz A, Sigmund O (1995) Checkerboard patterns in layout optimization. Struct Optim 10(1):40–45. https://doi.org/10.1007/BF01743693

Feil R, Pflumm T, Bortolotti P, Morandini M (2020) A cross-sectional aeroelastic analysis and structural optimization tool for slender composite structures. Compos Struct 253(112):755. https://doi.org/10.1016/j.compstruct.2020.112755

Ferrari F, Sigmund O, Guest JK (2021) Topology optimization with linearized buckling criteria in 250 lines of matlab. Struct Multidiscip Optim 63(6):3045–3066. https://doi.org/10.1007/s00158-021-02854-x

Gao X, Ma H (2015) Topology optimization of continuum structures under buckling constraints. Comput Struct 157:142–152. https://doi.org/10.1016/j.compstruc.2015.05.020

Giavotto V, Borri M, Mantegazza P, Ghiringhelli G, Carmaschi V, Maffioli GC, Mussi F (1983) Anisotropic beam theory and applications. Comput Struct 16(1):403–413. https://doi.org/10.1016/0045-7949(83)90179-7

Griffiths DR, Miles JC (2003) Determining the optimal cross-section of beams. Adv Eng Inform 17(2):59–76. https://doi.org/10.1016/S1474-0346(03)00039-9

Guest JK, Prévost JH, Belytschko T (2004) Achieving minimum length scale in topology optimization using nodal design variables and projection functions. Int J Numer Methods Eng 61(2):238–254. https://doi.org/10.1002/nme.1064

Guo X, Zhang W, Zhong W (2014) Doing topology optimization explicitly and geometrically—a new moving morphable components based framework. J Appl Mech. https://doi.org/10.1115/1.4027609

Guo G, Zhao Y, Su W, Zuo W (2021) Topology optimization of thin-walled cross section using moving morphable components approach. Struct Multidiscip Optim 63(5):2159–2176. https://doi.org/10.1007/s00158-020-02792-0

Han S (2022) Sensitivity analysis for sectional stiffness of anisotropic beams: the direct and adjoint methods. Compos Struct 285(115):215. https://doi.org/10.1016/j.compstruct.2022.115215

Hodges DH (2006) Nonlinear composite beam theory. Progress in astronautics and aeronautics, American Institute of Aeronautics and Astronautics.https://doi.org/10.2514/4.866821

Holmberg E, Torstenfelt B, Klarbring A (2013) Stress constrained topology optimization. Struct Multidiscip Optim 48(1):33–47. https://doi.org/10.1007/s00158-012-0880-7

Huang X, Xie M (2010) Evolutionary topology optimization of continuum structures: methods and applications. Wiley, Hoboken

Huang X, Xie YM (2010) A further review of ESO type methods for topology optimization. Struct Multidiscip Optim 41(5):671–683. https://doi.org/10.1007/s00158-010-0487-9

Kim YY, Kim TS (2000) Topology optimization of beam cross sections. Int J Solids Struct 37(3):477–493. https://doi.org/10.1016/S0020-7683(99)00015-3

Kim TS, Kim YY (2002) Multiobjective topology optimization of a beam under torsion and distortion. AIAA J 40(2):376–381. https://doi.org/10.2514/2.1656

Kostopoulos C, Marzok A, Waisman H (2025) Topology optimization of beams' cross-sectional properties considering torsional and warping behavior. Struct Multidiscip Optim 68(2):28. https://doi.org/10.1007/s00158-024-03952-2

Le C, Norato J, Bruns T, Ha C, Tortorelli D (2010) Stress-based topology optimization for continua. Struct Multidiscip Optim 41(4):605–620. https://doi.org/10.1007/s00158-009-0440-y

Leng J, Guest JK, Schafer BW (2011) Shape optimization of cold-formed steel columns. Thin-Walled Struct 49(12):1492–1503. https://doi.org/10.1016/j.tws.2011.07.009

Li Q, Qu Y, Luo Y, Liu S (2021) Concurrent topology optimization design of stiffener layout and cross-section for thin-walled structures. Acta Mech Sin 37(3):472–481. https://doi.org/10.1007/s10409-020-01034-2

Liu J, Li Q, Liu S, Tong L (2018) Dynamic topology optimization design of rotating beam cross-section with gyroscopic effects. Struct Multidiscip Optim 58(4):1467–1487. https://doi.org/10.1007/s00158-018-1974-7

Liu J, Li Q, Liu S, Tong L (2019) Concurrent optimization design of axial shape and cross-sectional topology for beam structures. Struct Multidiscip Optim 59(6):2287–2302. https://doi.org/10.1007/s00158-019-02195-w

Liu S, An X, Jia H (2008) Topology optimization of beam cross-section considering warping deformation. Struct Multidiscip Optim 35(5):403–411. https://doi.org/10.1007/s00158-007-0138-y

Luo Y, Chen W, Liu S, Li Q, Ma Y (2020) A discrete-continuous parameterization (DCP) for concurrent optimization of structural topologies and continuous material orientations. Compos Struct 236(111):900. https://doi.org/10.1016/j.compstruct.2020.111900

Makky SM, Ghalib MA (1979) Design for minimum deflection. Eng Optim 4(1):9–13. https://doi.org/10.1080/03052157908902400

Marzok A (2025) Simultaneous sizing and topology optimization of extruded elastic thin-walled beams. Comput Struct 311(107):689. https://doi.org/10.1016/j.compstruc.2025.107689

Marzok A, Waisman H (2023) XFEM based method for buckling analysis of thin-walled beams. Thin-Walled Struct 189(110):942. https://doi.org/10.1016/j.tws.2023.110942

Marzok A, Waisman H (2024) Topology optimization of extruded beams modeled with the XFEM for maximizing their natural frequencies. Mech Res Commun 135(104):234. https://doi.org/10.1016/j.mechrescom.2023.104234

Marzok A, Waisman H (2024) XFEM \ GFEM based approach for topology optimization of extruded beams with enhanced buckling resistance. Comput Methods Appl Mech Eng 418(116):541. https://doi.org/10.1016/j.cma.2023.116541

Marzok A, DeGanyar T, Waisman H (2023) Efficient XFEM approach for the analysis of thin-walled beams. Eng Struct 285(116):068. https://doi.org/10.1016/j.engstruct.2023.116068

Morandini M, Chierichetti M, Mantegazza P (2010) Characteristic behavior of prismatic anisotropic beam via generalized eigenvectors. Int J Solids Struct 47(10):1327–1337. https://doi.org/10.1016/j.ijsolstr.2010.01.017

Nguyen HD, Jang GW, Kim DM, Kim YY (2018) Finite prism method based topology optimization of beam cross section for buckling load maximization. Struct Multidiscip Optim 57(1):55–70. https://doi.org/10.1007/s00158-017-1860-8

Qiu Z, Li Q, Luo Y, Liu S (2022) Concurrent topology and fiber orientation optimization method for fiber-reinforced composites based on composite additive manufacturing. Comput Methods Appl Mech Eng 395(114):962. https://doi.org/10.1016/j.cma.2022.114962

Ren Y, Jinwu X, Zheqi L, Tiantian Z (2016) A novel topology optimization method for composite beams. Proc Inst Mech Eng Part G J Aerospace Eng 230(7):1153–1163. https://doi.org/10.1177/0954410015605547

Rozvany GIN, Zhou M (1991) The COC algorithm, Part I: cross-section optimization or sizing. Comput Methods Appl Mech Eng 89(1):281–308. https://doi.org/10.1016/0045-7825(91)90045-8

Sharafi P, Teh LH, Hadi MNS (2014) Shape optimization of thin-walled steel sections using graph theory and ACO algorithm. J Constr Steel Res 101:331–341. https://doi.org/10.1016/j.jcsr.2014.05.026

Shimoda M, Liu Y, Ishikawa K (2020) Optimum shape design of thin-walled cross sections using a parameter-free optimization method. Thin-Walled Struct 148(106):603. https://doi.org/10.1016/j.tws.2020.106603

Svanberg K (1987) The method of moving asymptotes—a new method for structural optimization. Int J Numer Methods Eng 24(2):359–373. https://doi.org/10.1002/nme.1620240207

Van Dijk NP, Maute K, Langelaar M, Van Keulen F (2013) Level-set methods for structural topology optimization: a review. Struct Multidiscip Optim 48(3):437–472. https://doi.org/10.1007/s00158-013-0912-y

Wang MY, Wang X, Guo D (2003) A level set method for structural topology optimization. Comput Methods Appl Mech Eng 192(1):227–246. https://doi.org/10.1016/S0045-7825(02)00559-5

Wang F, Lazarov BS, Sigmund O (2011) On projection methods, convergence and robust formulations in topology optimization. Struct Multidiscip Optim 43(6):767–784. https://doi.org/10.1007/s00158-010-0602-y

Wang Z, Suiker AS, Hofmeyer H, van Hooff T, Blocken B (2020) Coupled aerostructural shape and topology optimization of horizontal-axis wind turbine rotor blades. Energy Convers Manage 212(112):621. https://doi.org/10.1016/j.enconman.2020.112621

Wang Z, Suiker AS, Hofmeyer H, van Hooff T, Blocken B (2021) Optimization of thin-walled beam structures: Monolithic versus staggered solution schemes. Thin-Walled Struct 159(107):182. https://doi.org/10.1016/j.tws.2020.107182

Wang Z, Suiker AS, Hofmeyer H, van Hooff T, Blocken B (2021) Sequentially coupled shape and topology optimization for 2.5D and 3D beam models. Acta Mech 232(4):1683–1708. https://doi.org/10.1007/s00707-020-02930-1

Wu J, Sigmund O, Groen JP (2021) Topology optimization of multi-scale structures: a review. Struct Multidiscip Optim 63(3):1455–1480. https://doi.org/10.1007/s00158-021-02881-8

Yang RJ, Chen CJ (1996) Stress-based topology optimization. Struct Optim 12(2):98–105. https://doi.org/10.1007/BF01196941

Yang D, Liu H, Zhang W, Li S (2018) Stress-constrained topology optimization based on maximum stress measures. Comput Struct 198:23–39. https://doi.org/10.1016/j.compstruc.2018.01.008

Zargham S, Ward TA, Ramli R, Badruddin IA (2016) Topology optimization: a review for structural designs under vibration problems. Struct Multidiscip Optim 53(6):1157–1177. https://doi.org/10.1007/s00158-015-1370-5

Publisher's Note Springer Nature remains neutral with regard to jurisdictional claims in published maps and institutional affiliations.